

Tensor Non-Gaussianity from Axion-Gauge-Fields Dynamics: Parameter Search

Aniket Agrawal,^a Tomohiro Fujita^b Eiichiro Komatsu^{a,c}

^aMax-Planck-Institut für Astrophysik, Karl-Schwarzschild-Str. 1, 85741 Garching, Germany

^bDepartment of Physics, Kyoto University, Kyoto 606-8502, Japan

^cKavli Institute for the Physics and Mathematics of the Universe, Todai Institutes for Advanced Study, the University of Tokyo, Kashiwa, Japan 277-8583 (Kavli IPMU, WPI)

E-mail: aniket@mpa-garching.mpg.de, t.fujita@tap.scphys.kyoto-u.ac.jp,
komatsu@mpa-garching.mpg.de

Abstract. We calculate the bispectrum of scale-invariant tensor modes sourced by spectator SU(2) gauge fields during inflation in a model containing a scalar inflaton, a pseudoscalar axion and SU(2) gauge fields. A large bispectrum is generated in this model at tree-level as the gauge fields contain a tensor degree of freedom, and its production is dominated by self-coupling of the gauge fields. This is a unique feature of non-Abelian gauge theory. The shape of the tensor bispectrum is approximately an equilateral shape for $3 \lesssim m_Q \lesssim 4$, where m_Q is an effective dimensionless mass of the SU(2) field normalised by the Hubble expansion rate during inflation. The amplitude of non-Gaussianity of the tensor modes, characterised by the ratio B_h/P_h^2 , is inversely proportional to the energy density fraction of the gauge field. This ratio can be much greater than unity, whereas the ratio from the vacuum fluctuation of the metric is of order unity. The bispectrum is effective at constraining large m_Q regions of the parameter space, whereas the power spectrum constrains small m_Q regions.

Contents

1	Introduction	1
2	Model Setup	2
3	Amplification of Gravitational Waves	4
4	Bispectrum of Gravitational Waves	7
4.1	Diagram (i)	8
4.2	Diagram (ii)	12
4.3	Diagram (iii)	14
4.4	Total bispectrum	17
5	Peak of Bispectrum	21
6	Parameter Search	23
6.1	Tensor-to-scalar ratio	24
6.2	Tensor bispectrum	24
6.3	Consistency of the model	25
6.4	Allowed parameter regions	25
7	Conclusion	26
A	Polarisation Tensor	27
B	Equilateral Shape	30

1 Introduction

We do not yet know how to quantize gravity over an entire spacetime, but we can quantize its perturbations around a specified background. In this case, the degrees of freedom of the gravitational field, including the transverse traceless tensor modes of the metric, should have ground state vacuum fluctuations [1, 2]. These can be found in B-mode polarisation of the cosmic microwave background (CMB) [3, 4]; thus, a detection of non-zero (primordial) B-modes is evidence for tensor fluctuations of the metric.

So far, no such evidence has been found [5]. CMB experiments provide constraints on the tensor-to-scalar ratio r , which is defined as the ratio of the power in tensor modes ($P_h(k_0)$) to the power in scalar modes ($P_\zeta(k_0)$), at some wavenumber k_0 , $r \equiv P_h(k_0)/P_\zeta(k_0)$. Currently, this ratio is constrained to be $r < 0.07$ (95 % C.L.) [5] at $k_0 = 0.05 \text{ Mpc}^{-1}$.

We stress here that a detection of B-mode polarisation in the CMB is evidence for primordial tensor perturbations, but is not necessarily evidence for the vacuum fluctuation in the tensor metric. For the standard scenario of single-field slow-roll inflation, the tensor fluctuations of the metric, h_{ij} , obey the equation

$$\square h_{ij}(t, \mathbf{x}) = 0, \tag{1.1}$$

where \square is the d'Alembertian operator in 4-dimensions. Equation (1.1) shows that if we find evidence for tensor fluctuations, in the absence of anything that can source them, they have to be necessarily quantum.

However, there is no *a priori* reason to ignore sources in the right hand side of Equation (1.1). It is reasonable to think that there are (many) more than one field during inflation. While their energy density may be much smaller than that of the dominant inflaton field, they can still act as sources of perturbations. In general, we write

$$\square h_{ij}(t, \mathbf{x}) = \Pi_{ij}(t, \mathbf{x}), \quad (1.2)$$

and tensor perturbations are sourced by the anisotropic stress-energy Π_{ij} , which is provided by quantum fluctuations of a field other than the metric. These sourced tensor fluctuations can be much larger than the vacuum one and can generate observable B-modes, invalidating the claim that B-modes are evidence for vacuum fluctuations of the metric. Consequently, there have been intense efforts to build inflation models where a sizeable r can be generated from sources, without violating stringent observational constraints on the scalar perturbation. The sources include scalars [6–9], U(1) gauge fields [10–14], and SU(2) gauge fields [15–22].

How then, do we differentiate between B-modes generated from vacuum fluctuations of the metric and those from sources? Vacuum fluctuations of the metric are usually almost scale invariant, with a slightly red tilt (see [23] for the latest review). On the other hand, B-modes from sources can have a red or blue tilt or completely non-power-law spectra such as bumps, depending upon model parameters. Moreover, the tensor fluctuations produced by sources can be chiral (see section 3), and so can be seen as a non-vanishing TB/EB correlation in the CMB [24–29], whereas vacuum fluctuations produce parity-even B-modes. Finally, these modes can be highly non-Gaussian [30]. Because tensor modes from vacuum fluctuations of the metric are almost Gaussian [31, 32], non-Gaussianity provides strong evidence for sourced tensor modes. Therefore, we hope that in any future detections of primordial gravitational waves (GWs), one would not only check for their amplitude (r) and scale-invariance, but also their non-Gaussianity and parity-violating correlations. Only after *all* these tests support nearly scale-invariant, Gaussian, and non-chiral primordial B-modes, can we confidently claim to have discovered vacuum fluctuations of the metric.

We focused on a particular set of model parameters in ref. [30], using a model proposed by Dimastrogiovanni, Fasiello and Fujita [20]. In this paper we shall give more detailed derivations of the bispectrum and present the results for wider parameter space. The rest of the paper is organised as follows : in section 2 we present details of the model that we consider. In section 3 we present the second-order Lagrangian for the tensor perturbations in our model and their imprint on the B-mode power spectrum. The third-order Lagrangian is presented in section 4 and is used to calculate the bispectrum of metric fluctuations. A detailed discussion of the deviation of the bispectrum from the equilateral shape is given in section 5. In section 6 we explore parameter regions of the model, which can be potentially observed in upcoming CMB missions. We conclude in section 7.

2 Model Setup

In the model of ref. [20], inflation is driven by a scalar inflaton ϕ , which is only minimally coupled to a pseudoscalar axion χ and SU(2) gauge fields, A_μ^a . The SU(2) gauge fields and the axion have negligible energy densities compared to the inflaton, and thus are called

“spectator fields”. They are coupled to each other by a Chern-Simons like interaction $\chi F\tilde{F}$. The Lagrangian is then given as,

$$\mathcal{L} = \mathcal{L}_{\text{GR}} + \mathcal{L}_\phi + \mathcal{L}_{\text{spec}}, \quad (2.1)$$

$$\mathcal{L}_{\text{spec}} = -\frac{1}{2}(\partial\chi)^2 - V(\chi) - \frac{1}{4}F_{\mu\nu}^a F^{a\mu\nu} + \frac{\lambda\chi}{4f}F_{\mu\nu}^a \tilde{F}^{a\mu\nu}, \quad (2.2)$$

where Einstein gravity $\mathcal{L}_{\text{GR}} = M_{\text{p}}^2 R/2$ is assumed, the Lagrangian of the inflaton \mathcal{L}_ϕ is not specified, and $\mathcal{L}_{\text{spec}}$ denotes the Lagrangian of the spectator fields. $V(\chi)$ is the potential of the axion field with the canonical kinetic term $-(\partial\chi)^2/2$, the gauge field strength tensor $F_{\mu\nu}^a$ is written in terms of the gauge fields as $F_{\mu\nu}^a = \partial_\mu A_\nu^a - \partial_\nu A_\mu^a - g\epsilon^{abc}A_\mu^b A_\nu^c$ with g being the self-coupling constant, a dimensionless parameter λ controls the strength of the Chern-Simons interaction, f is a decay constant of the axion field, and $\tilde{F}^{a\mu\nu} \equiv \epsilon^{\mu\nu\rho\sigma} F_{\rho\sigma}^a / (2\sqrt{-g})$ is the dual of $F_{\mu\nu}^a$. In the rest of this section, we discuss the background dynamics, while perturbations will be studied in the following sections.

In this paper, we do not solve for the inflaton $\phi(t)$, but consider dynamics of the spectator fields in a de Sitter universe, where the Hubble expansion rate is constant. We also leave the axion potential $V(\chi)$ unspecified by assuming that it supports slow-roll of the background axion $\chi_0(t)$ with the aid of the coupling to the SU(2) fields. While these assumptions are far from generic, they still capture the essence of physics of generation of non-Gaussianity, and are observationally relevant because they produce scale-invariant GWs.

As shown in [33, 34], while the background axion slowly evolves, the homogeneous background component of the gauge fields has an attractor configuration which respects isotropy of the universe,

$$A_0^a = 0, \quad A_i^a = \delta_i^a a(t)Q(t), \quad (2.3)$$

where $a(t)$ is the scale factor. Then we decompose these spectator fields into the background and the perturbation components as

$$\chi(t, \mathbf{x}) = \chi_0(t) + \delta\chi(t, \mathbf{x}), \quad A_i^a(t, \mathbf{x}) = \delta_i^a a(t)Q(t) + \delta A_i^a(t, \mathbf{x}). \quad (2.4)$$

There also exist non-dynamical components δA_0^a that we integrate out. The equations of motion (EoM) for the background fields are given by

$$\ddot{\chi}_0 + 3H\dot{\chi}_0 + \partial_\chi V(\chi_0) = -\frac{3g\lambda}{f}Q^2 (\dot{Q} + HQ), \quad (2.5)$$

$$\ddot{Q} + 3H\dot{Q} + (\dot{H} + 2H^2)Q + 2g^2Q^3 = \frac{g\lambda}{f}Q^2\dot{\chi}_0, \quad (2.6)$$

where the dots denote cosmic time derivatives ∂_t and $H \equiv \dot{a}/a$ is the Hubble expansion rate. The terms on the right hand side of eq. (2.5) slow down the time evolution of $\chi_0(t)$ in addition to the Hubble friction term $3H\dot{\chi}_0$, because a non-zero background value $Q(t)$ is sustained by energy transfer from the kinetic energy of χ_0 through the coupling. Here we introduce two dimensionless parameters;

$$m_Q(t) \equiv \frac{gQ}{H}, \quad \Lambda(t) \equiv \frac{\lambda Q}{f}. \quad (2.7)$$

Here, m_Q is the effective mass of the SU(2) field around its vacuum expectation value (vev) normalized by the Hubble scale, and Λ characterizes the coupling strength between χ_0 and Q .

Note that the right hand side of eqs. (2.5) and (2.6) are proportional to $m_Q \Lambda$. We consider the slow-roll regime, $m_Q \gtrsim 1$ and $\Lambda \gg 1$, in which Q is stabilized by its effective mass and χ_0 is significantly slowed down by the coupling. We can then drop all the terms with time derivatives in the EoMs except for the r.h.s. of eq. (2.6) and find [33]

$$m_Q \simeq \left(\frac{-g^2 f \partial_\chi V(\chi_0)}{3\lambda H^4} \right)^{\frac{1}{3}}, \quad (2.8)$$

$$\xi \equiv \frac{\lambda \dot{\chi}_0}{2fH} \simeq m_Q + m_Q^{-1}. \quad (2.9)$$

The Einstein equations at the background yield

$$3M_{\text{P}}^2 H^2 = \rho_\phi + \frac{1}{2} \dot{\chi}_0 + V(\chi_0) + \frac{3}{2} (\dot{Q} + HQ)^2 + \frac{3}{2} g^2 Q^4, \quad (2.10)$$

$$-\frac{\dot{H}}{H^2} = \epsilon_\phi + \epsilon_\chi + \epsilon_B + \epsilon_E, \quad (2.11)$$

where ρ_ϕ is the energy density of the inflaton and the slow-roll parameters are defined as $\epsilon_\phi \equiv -\dot{\rho}_\phi/6M_{\text{P}}^2 H^3$, $\epsilon_\chi \equiv \dot{\chi}^2/2M_{\text{P}}^2 H^2$, $\epsilon_E \equiv (\dot{Q} + HQ)^2/M_{\text{P}}^2 H^2$, and $\epsilon_B \equiv g^2 Q^4/M_{\text{P}}^2 H^2$. We shall assume that ρ_ϕ dominates in eq. (2.10). In the slow-roll regime, $\dot{Q} \ll HQ$, one finds

$$\epsilon_E \simeq \frac{\epsilon_B}{m_Q^2}. \quad (2.12)$$

The background fields appear only through H, m_Q, ξ, ϵ_E and ϵ_B in the EoMs for the perturbations. Using the relationships, eqs. (2.9) and (2.12), one can eliminate ξ and ϵ_E . Furthermore, in the slow-roll regime, one can disregard the time variations of H, m_Q and ϵ_B in the leading order approximation. Therefore we have three relevant background parameters H, m_Q and ϵ_B which are approximated to be constant in this paper.¹

3 Amplification of Gravitational Waves

In this section, we study the tensor perturbations at linear level. Only the tensor perturbations are amplified due to tachyonic instability, while scalar and vector perturbations are not amplified for $m_Q > \sqrt{2}$ in this model [35]. Although the scalar perturbations of χ and A_i^a are generated from the vacuum fluctuations, their contribution to the curvature perturbation ζ is negligible, unless the energy density of χ becomes comparable to that of the inflaton after inflation [20].² The vector perturbations decay on super-horizon scales in any case. Therefore in this paper, we assume that the observed curvature perturbation was produced from the inflaton fluctuation $\delta\phi$ and concentrate on the tensor perturbations from the gauge fields.

¹In ref. [20], the background dynamics is numerically solved, and the perturbations are also solved with the time varying background quantities, $m_Q(t), \epsilon_B(t)$ and $H(t)$. They find that $m_Q, \epsilon_B, H \approx \text{const.}$ is a very good approximation for a sufficiently strong coupling, especially when one is interested in the range of wavenumbers observable by CMB.

²The scalar perturbations of χ and A_i^a directly contribute to ζ through the density perturbation (e.g. $\delta\rho_\chi \simeq \partial_\chi V \delta\chi$). This channel is negligible, for instance, if χ reaches its potential minimum (i.e. $V(\chi), \partial_\chi V(\chi) \rightarrow 0$) during inflation. If χ_0 acquires a non-negligible energy fraction after inflation, however, the contribution to ζ from $\delta\chi$ may be relevant. This implies that the spectator sector can produce ζ in a way similar to the curvaton mechanism [36, 37]. We leave this intriguing possibility for future work.

To calculate the power spectrum and bispectrum of GWs we need to expand the action, equation (2.1), up to second and third order in perturbations, respectively. We write the tensor perturbations of the metric and the SU(2) gauge field [17, 35] as:

$$g_{ij} = -a^2(\delta_{ij} + h_{ij}), \quad \delta A_i^a = t_{ai} + \dots, \quad (3.1)$$

where \dots represents the scalar and vector perturbations of the SU(2) gauge fields which we neglect in this paper. We have imposed the transverse and traceless conditions on h_{ij} and t_{ij} , $\delta^{ij}\mathcal{T}_{ij} = \partial_i\mathcal{T}_{ij} = \partial_j\mathcal{T}_{ij} = 0$ ($\mathcal{T} = h$ and t). The inverse metric is given by $g^{ij} = -a^{-2}(\delta^{ij} - h^{ij} + h^{ik}h^{kj} + \mathcal{O}(h^3))$. For later convenience, we redefine h_{ij} as

$$\psi_{ij} = \frac{1}{2}aM_{\text{P}}h_{ij}. \quad (3.2)$$

Precisely speaking t_{ai} is not a tensor, since the index a is not a spatial index but the label of SU(2) gauge. Nonetheless, under the background configuration of eq. (2.3), t_{ai} transforms as a tensor in practice, because the gauge index a is identified with a spatial index.

Substituting these in equation (2.1), and expanding up to third order, we obtain the Lagrangian of the tensor perturbations as

$$S_{\text{tensor}} = \int d\tau d^3x \sqrt{-g} \left[L_2 + L_3^{(i)} + L_3^{(ii)} + L_3^{(iii)} \right], \quad (3.3)$$

with [38]

$$\begin{aligned} L_2 = & \frac{1}{2}\psi'_{ij}\psi'_{ij} - \frac{1}{2}\partial_k\psi_{ij}\partial_k\psi_{ij} + \frac{1}{\tau^2}\psi_{ij}\psi_{ij} + \frac{1}{2}t'_{ij}t'_{ij} - \frac{1}{2}\partial_l t_{ij}\partial_l t_{ij} + \frac{2m_Q + m_Q^{-1}}{\tau}\epsilon^{ijk}t_{il}\partial_j t_{kl} \\ & - \frac{m_Q^2 + 1}{\tau^2}t_{ij}t_{ij} + \frac{2\sqrt{\epsilon_B}}{\tau} \left[\frac{1}{m_Q}\psi_{ij}t'_{ij} - \psi_{jm}\epsilon_{aij}\partial_i t_{am} + \frac{m_Q}{\tau}\psi_{ij}t_{ij} \right], \end{aligned} \quad (3.4)$$

where $\tau \simeq -1/aH$ is the conformal time, prime denotes the derivative with respect to τ and we neglect terms suppressed by slow-roll parameters. The cubic Lagrangian L_3 will be discussed in the next section.

From the quadratic Lagrangian above, we obtain the following EoMs for GWs $\psi_{ij}(\tau, \mathbf{x})$ and tensor perturbations of the SU(2) gauge field $t_{ij}(\tau, \mathbf{x})$,

$$\psi''_{ij} - \partial_k^2\psi_{ij} - \frac{2}{\tau^2}\psi_{ij} = \frac{2\sqrt{\epsilon_B}}{m_Q\tau}t'_{ij} + \frac{2\sqrt{\epsilon_B}}{\tau}\epsilon^{api}\partial_p t_{aj} + \frac{2\sqrt{\epsilon_B}m_Q}{\tau^2}t_{ij}, \quad (3.5)$$

$$t''_{ij} - \partial_k^2 t_{ij} + \frac{2(2m_Q + m_Q^{-1})}{\tau}\epsilon^{lkj}\partial_k t_{il} + \frac{2(m_Q^2 + 1)}{\tau^2}t_{ij} = \mathcal{O}(\psi_{ij}). \quad (3.6)$$

Although terms linear in ψ_{ij} also source the gauge field t_{ij} , ψ_{ij} is not as substantially amplified as t_{ij} [17–20], and so we ignore its contribution as a source for t_{ij} . To solve the dynamics of ψ_{ij} and t_{ij} , it is useful to decompose them with the circular polarisation tensors,

$$X_{ij}(\tau, \mathbf{x}) = \int \frac{d^3k}{(2\pi)^3} e^{i\mathbf{k}\cdot\mathbf{x}} \left[e_{ij}^R(\mathbf{k})X_{\mathbf{k}}^R(\tau) + e_{ij}^L(\mathbf{k})X_{\mathbf{k}}^L(\tau) \right], \quad (3.7)$$

where $X = \psi, t$ and the properties of the polarisation tensors are summarized in appendix. A. Note that we normalize e_{ij}^p such that $e_{ij}^R(\mathbf{k})e_{ij}^R(-\mathbf{k}) = e_{ij}^L(\mathbf{k})e_{ij}^L(-\mathbf{k}) = 1$.

To proceed further, we quantize ψ and t and expand them in a perturbative series as [39]

$$\hat{X}_{\mathbf{k}}^p(\tau) = \hat{X}_1^p(\tau, \mathbf{k}) + \hat{X}_2^p(\tau, \mathbf{k}) + \dots \quad (3.8)$$

The first order components are written as

$$\hat{t}_1^p(\tau, \mathbf{k}) = T_1^p(\tau, k) \hat{a}_{\mathbf{k}}^p + T_1^{p*}(\tau, k) \hat{a}_{-\mathbf{k}}^{p\dagger}, \quad (3.9)$$

$$\hat{\psi}_1^p(\tau, \mathbf{k}) = \Psi_1^p(\tau, k) \hat{a}_{\mathbf{k}}^p + \Psi_1^{p*}(\tau, k) \hat{a}_{-\mathbf{k}}^{p\dagger}, \quad (3.10)$$

with the creation/annihilation operators, $\hat{a}_{\mathbf{k}}^p$ and $\hat{a}_{\mathbf{k}}^{p\dagger}$, satisfying $[\hat{a}_{\mathbf{k}}^p, \hat{a}_{-\mathbf{k}'}^{q\dagger}] = (2\pi)^3 \delta^{pq} \delta(\mathbf{k} + \mathbf{k}')$. We only consider GWs sourced by the gauge field in this paper, and assign $\hat{\psi}_1$ the same quantum operator as \hat{t}_1 . The mode functions of \hat{X}_1^p satisfy linearised EoMs and their solutions induce the second order fields \hat{X}_2^p through non-linear terms in the EoMs.

In Fourier space the EoMs for the linear mode functions can be written as,

$$\partial_x^2 T_1^{R/L} + \left[1 \mp \frac{2(2m_Q + m_Q^{-1})}{x} + \frac{2(m_Q^2 + 1)}{x^2} \right] T_1^{R/L} = \mathcal{O}(\Psi_1^{R/L}), \quad (3.11)$$

$$\partial_x^2 \Psi_1^{R/L} + \left[1 - \frac{2}{x^2} \right] \Psi_1^{R/L} = \frac{2\sqrt{\epsilon_B}}{m_Q x} \partial_x T_1^{R/L} \mp \frac{2\sqrt{\epsilon_B}}{x} T_1^{R/L} + \frac{2\sqrt{\epsilon_B} m_Q}{x^2} T_1^{R/L}, \quad (3.12)$$

where $x \equiv -k\tau$. The minus and plus signs are for right- (R) and left-handed (L) modes, respectively. Only T_1^R undergoes an instability and it sources only Ψ_1^R [15, 18, 19, 33], provided that m_Q is positive. Therefore, we only consider the right-handed polarisation in the rest of the paper. The homogeneous solution for T_1^R can be analytically calculated and is expressed in terms of the Whittaker function $W_{\beta, \alpha}(z)$ as

$$T_1^R(\tau, k) = \frac{1}{\sqrt{2k}} e^{\frac{\pi}{2}(2m_Q + m_Q^{-1})} W_{\beta, \alpha}(2ik\tau), \quad (3.13)$$

where $\alpha \equiv -i\sqrt{2m_Q^2 + 7/4}$ and $\beta \equiv -i(2m_Q + m_Q^{-1})$ [15, 17, 20]. Ψ_1^R can then be calculated using Green's function method,

$$\Psi_1^R(\tau, \mathbf{k}) = \int_{-\infty}^{\infty} d\eta G_\psi(\tau, \eta, k) \mathcal{D}(\eta, k) T_1^R(\eta, k), \quad (3.14)$$

with

$$G_\psi(\tau, \eta, k) = \frac{\Theta(\tau - \eta)}{k^3 \tau \eta} \left[k(\eta - \tau) \cos(k(\tau - \eta)) + (1 + k^2 \tau \eta) \sin(k(\tau - \eta)) \right], \quad (3.15)$$

$$\mathcal{D}(\eta, k) = \frac{2\sqrt{\epsilon_B}}{m_Q \eta} \partial_\eta + \frac{2\sqrt{\epsilon_B}}{\eta^2} (m_Q + k\eta), \quad (3.16)$$

where $\Theta(x)$ is the unit Heaviside function of x . In figure 1, we plot T_1^R , the source term $\mathcal{D}T_1^R$, Green's function G_ψ in the super-horizon limit and the sourced gravitational wave Ψ_1^R . The time integral of the source term $\mathcal{D}T_1^R$ multiplied by G_ψ yields Ψ_1^R . The source term $\mathcal{D}T_1^R$ peaks around the horizon crossing and Green's function stops oscillating there. As a result, Ψ_1^R is mainly produced around the horizon crossing as well, as seen in the right panel.

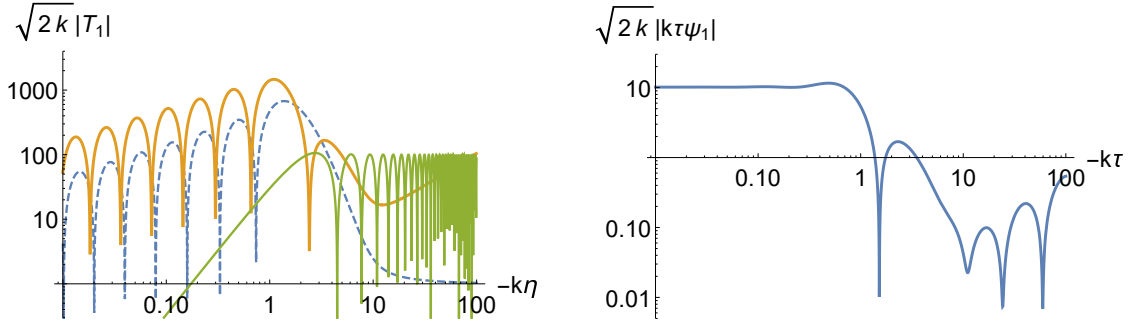


Figure 1: (Left panel) We plot the linear gauge tensor mode function $\sqrt{2k}|T_1^R(\eta, k)|$ (blue dashed), the source terms $\sqrt{2k}|m_Q^{-1}\eta\partial_\eta T_1 + (m_Q + k\eta)T_1|$ (orange solid) and $10|k\eta \cos(k\eta) - \sin(k\eta)|$ which is proportional to Green's function $G_\psi(\tau, \eta, k)$ in the super-horizon limit, $-k\tau \rightarrow 0$, multiplied by 10 for illustrative purpose (green solid). **(Right panel)** The sourced linear gravitational wave $\sqrt{2k}|k\tau\Psi_1^R(\tau, k)|$ is shown. $|\Psi_1^R|$ grows significantly around the horizon-crossing ($-k\tau \sim 1$) and stays constant on super-horizon scales. In both panels, we set $m_Q = 3.15$ and $\epsilon_B = 3 \times 10^{-4}$.

Equation (3.14) can also be analytically solved and in the super-horizon limit we obtain,

$$\lim_{|k\tau| \rightarrow 0} \Psi_1^R(\tau, \mathbf{k}) = \frac{\sqrt{\epsilon_B}}{\sqrt{2k}k\tau} \mathcal{F}(m_Q), \quad (3.17)$$

from which we obtain the power spectrum of h in the super-horizon limit [20]

$$\frac{k^3}{2\pi^2} P_h^{\text{sourced}} = \frac{\epsilon_B H^2}{\pi^2 M_P^2} |\mathcal{F}(m_Q)|^2, \quad (3.18)$$

where \mathcal{F} is a function of m_Q , whose exact expression is given in [20] ($\mathcal{F}(m_Q)$ here is $\mathcal{F}_B + \mathcal{F}_E/m_Q$ there). The function $\mathcal{F}(m_Q)$ can be approximated to be an exponential function of m_Q , $|\mathcal{F}(m_Q)| \approx e^{1.8m_Q}$. Note that eq. (3.18) is derived under the assumption of $(m_Q, \epsilon_B, H) = \text{const}$. However, as long as the time variations of these background quantities are slow, eq. (3.18) with $m_Q(t), \epsilon_B(t), H(t)$ at the horizon crossing time $k = a(t)H(t)$ gives a good approximation of $P_h^{\text{sourced}}(k)$. It should be also noted that only the right-handed polarisation modes contribute to the above $P_h^{\text{sourced}}(k)$.

4 Bispectrum of Gravitational Waves

In this section, we calculate the tensor bispectrum of the right-handed GWs, B_h^{RRR} , in the super-horizon limit:

$$\begin{aligned} (2\pi)^3 \delta(\mathbf{k}_1 + \mathbf{k}_2 + \mathbf{k}_3) B_h^{RRR}(k_1, k_2, k_3) &= \lim_{\tau \rightarrow 0} \left\langle \hat{h}^R(\tau, \mathbf{k}_1) \hat{h}^R(\tau, \mathbf{k}_2) \hat{h}^R(\tau, \mathbf{k}_3) \right\rangle, \\ &= \lim_{\tau \rightarrow 0} \left(\frac{2}{aM_P} \right)^3 \left\langle \hat{\psi}^R(\tau, \mathbf{k}_1) \hat{\psi}^R(\tau, \mathbf{k}_2) \hat{\psi}^R(\tau, \mathbf{k}_3) \right\rangle. \end{aligned} \quad (4.1)$$

The three-point correlator of the right-handed GWs $\hat{\psi}^R = \hat{\psi}_1^R + \hat{\psi}_2^R$ can be written as

$$\begin{aligned} \langle \hat{\psi}^R(\tau, \mathbf{k}_1) \hat{\psi}^R(\tau, \mathbf{k}_2) \hat{\psi}^R(\tau, \mathbf{k}_3) \rangle &= \langle \hat{\psi}_1^R(\tau, \mathbf{k}_1) \hat{\psi}_1^R(\tau, \mathbf{k}_2) \hat{\psi}_2^R(\tau, \mathbf{k}_3) \rangle \\ &+ \langle \hat{\psi}_1^R(\tau, \mathbf{k}_1) \hat{\psi}_2^R(\tau, \mathbf{k}_2) \hat{\psi}_1^R(\tau, \mathbf{k}_3) \rangle + \langle \hat{\psi}_2^R(\tau, \mathbf{k}_1) \hat{\psi}_1^R(\tau, \mathbf{k}_2) \hat{\psi}_1^R(\tau, \mathbf{k}_3) \rangle, \end{aligned} \quad (4.2)$$

because $\hat{\psi}_1^R$ satisfies Gaussian statistics. We calculate $\hat{\psi}_2$ using the second order EoMs for the tensor perturbations which are derived from the cubic Lagrangian.

The cubic tensor Lagrangians introduced in eq. (3.3) are given by

$$L_3^{(i)} = c^{(i)} \left[\epsilon^{abc} t_{ai} t_{bj} \left(\partial_i t_{cj} - \frac{m_Q^2 + 1}{3m_Q \tau} \epsilon^{ijk} t_{ck} \right) - \frac{m_Q}{\tau} t_{ij} t_{jl} t_{li} \right], \quad (4.3)$$

$$\begin{aligned} L_3^{(ii)} = c^{(ii)} \psi_{ij} &\left[\frac{\tau}{2m_Q} \left\{ t'_{il} t'_{jl} - \partial_i t_{kl} (\partial_j t_{kl} - 2\partial_k t_{jl}) - \partial_k t_{il} \partial_l t_{jl} \right\} \right. \\ &\left. - \epsilon^{iab} t_{al} (\partial_j t_{bl} - \partial_l t_{bj}) - \epsilon^{lab} t_{ai} \partial_l t_{bj} - \frac{3m_Q}{2\tau} t_{il} t_{jl} \right], \end{aligned} \quad (4.4)$$

$$L_3^{(iii)} = c^{(iii)} \psi_{ij} \left[\frac{1}{m_Q} \psi_{jk} t'_{ik} + \epsilon^{ajm} \psi_{lm} \partial_i t_{al} - \psi_{jk} \epsilon^{akl} \partial_l t_{ai} \right], \quad (4.5)$$

where we organize terms such that $L_3^{(i)} = \mathcal{O}(t^3)$, $L_3^{(ii)} = \mathcal{O}(\psi t^2)$ and $L_3^{(iii)} = \mathcal{O}(\psi^2 t)$ and we neglect the $\mathcal{O}(\psi^3)$ terms. The coefficients of the cubic Lagrangians are

$$c^{(i)} = g = \frac{m_Q^2 H}{\sqrt{\epsilon_B} M_{\text{Pl}}}, \quad c^{(ii)} = \frac{2m_Q H}{M_{\text{Pl}}}, \quad c^{(iii)} = \frac{4\sqrt{\epsilon_B} H}{M_{\text{Pl}}}. \quad (4.6)$$

They satisfy a hierarchical relationship,

$$\frac{c^{(ii)}}{c^{(i)}} = \frac{c^{(iii)}}{c^{(ii)}} = \frac{2\sqrt{\epsilon_B}}{m_Q} \ll 1. \quad (4.7)$$

The tree-level contributions from $L_3^{(i)}$, $L_3^{(ii)}$ and $L_3^{(iii)}$ to the tensor bispectrum are illustrated as Feynman diagrams in figure 2. As we see below, the contributions from the three diagrams to the gravitational wave bispectrum are also hierarchical, $(i) > (ii) \gg (iii)$.³ In what follows, we calculate these three contributions in order. When we show plots in this section, we use the following parameters as an example,

$$H = 8 \times 10^{12} \text{GeV}, \quad m_Q = 3.15, \quad \epsilon_B = 3 \times 10^{-4}. \quad (4.8)$$

The viable parameter space will be explored in section. 6.

4.1 Diagram (i)

This diagram arises from the self-interaction of the SU(2) gauge field, and thus is absent in Abelian theory. Here, the second order gravitational wave $\hat{\psi}_2^R$ is sourced linearly by \hat{t}_2^R , but the second order gauge field perturbation \hat{t}_2^R is produced by \hat{t}_1^R via non-linearity. The

³The diagram (ii) includes only two circled crosses which carry a small parameter $\sqrt{\epsilon_B}$, while the diagram (i) includes three. Hence, in spite of the hierarchical vertex coefficients $c^{(i)} \gg c^{(ii)}$, their contributions are comparable.

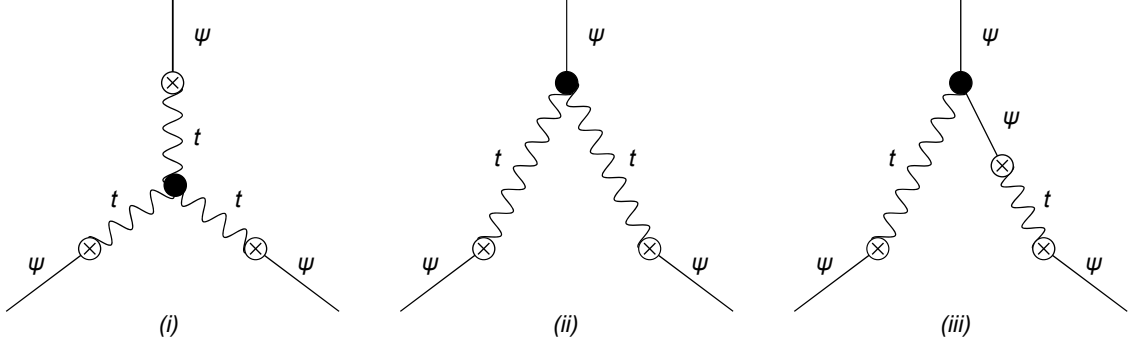


Figure 2: Feynman diagrams illustrating the tree-level contributions from the cubic interactions $L_3^{(i)}$, $L_3^{(ii)}$ and $L_3^{(iii)}$ to the bispectrum of GWs. The straight and wavy lines show ψ_{ij} and t_{ij} , respectively. The black dots show the vertices of the three-point interactions, while the circled crosses show the mixing between ψ_{ij} and t_{ij} (the last term in Eq. (3.4)).

cubic Lagrangian $L_3^{(i)}$ gives the source term $\mathcal{S}_{ij}^{(i)}$ in the EoM for the second order gauge field perturbation,

$$t''_{ij}(\tau, \mathbf{x}) - \partial_k^2 t_{ij}(\tau, \mathbf{x}) + \frac{2(2m_Q + m_Q^{-1})}{\tau} \epsilon^{lkj} \partial_k t_{il}(\tau, \mathbf{x}) + \frac{2(m_Q^2 + m_Q^{-1})}{\tau^2} t_{ij}(\tau, \mathbf{x}) = \mathcal{S}_{ij}^{(i)}, \quad (4.9)$$

$$\mathcal{S}_{ij}^{(i)} = \frac{\delta L_3^{(i)}}{\delta t_{ij}} = 2g\epsilon^{aic} t_{al} \partial_l t_{cj} - g\epsilon^{aic} t_{al} \partial_j t_{cl} - \frac{3gm_Q}{\tau} t_{ip} t_{pj} - \frac{g\xi}{\tau} \epsilon^{ibc} \epsilon^{jmn} t_{bm} t_{cn}, \quad (4.10)$$

where the source term $\mathcal{S}_{ij}^{(i)}$ is evaluated with the first order solution $\hat{t}_1^R(\tau, \mathbf{k})$. Although in second order it is no longer true that the right-handed polarisation is sourced only by the right-handed tensors, the exponential amplification of the right-handed modes ensures that terms containing the left-handed modes are exponentially smaller. Thus we only use the right-handed polarisation of the gauge field perturbation to evaluate the source term. Note that this source term contains g explicitly because of the non-Abelian nature of the vertex.

Expanding the tensor perturbation with the tensor polarisation as before, one finds the EoM in Fourier space as

$$\hat{t}_2^{R}(\tau, \mathbf{k}) + \left(1 + \frac{2(m_Q^2 + m_Q^{-1})}{\tau^2} + 2k \frac{2m_Q + m_Q^{-1}}{\tau}\right) \hat{t}_2^R(\tau, \mathbf{k}) = g e_{ij}^L(\mathbf{k}) \int \int \frac{d^3 q_1}{(2\pi)^3} \frac{d^3 q_2}{(2\pi)^3} \delta_D(\mathbf{q}_1 + \mathbf{q}_2 - \mathbf{k}) Q_{ij}^{(i)}(\mathbf{q}_1, \mathbf{q}_2, \tau) \hat{t}_1^R(\mathbf{q}_1, \tau) \hat{t}_1^R(\mathbf{q}_2, \tau), \quad (4.11)$$

where we have substituted $[e_{ij}^R(\mathbf{k})]^{-1} = e_{ij}^L(\mathbf{k})$ and

$$Q_{ij}^{(i)}(\mathbf{q}_1, \mathbf{q}_2, \tau) = 2i\epsilon^{aic} e_{al}^R(\mathbf{q}_1) e_{cj}^R(\mathbf{q}_2) q_{2l} - i\epsilon^{aic} e_{al}^R(\mathbf{q}_1) e_{cl}^R(\mathbf{q}_2) q_{2j} - \frac{3m_Q}{\tau} e_{ik}^R(\mathbf{q}_1) e_{kj}^R(\mathbf{q}_2) - \frac{m_Q + m_Q^{-1}}{\tau} \epsilon^{ibc} \epsilon^{jmn} e_{bm}^R(\mathbf{q}_1) e_{cn}^R(\mathbf{q}_2). \quad (4.12)$$

Using the homogeneous solution, equation (3.13), Green's function for equation (4.11) can

be written as [39],

$$G_t(\tau, \eta, k) = i\Theta(\tau - \eta) [T_1^R(\tau, \mathbf{k})T_1^{*R}(\eta, \mathbf{k}) - T_1^{*R}(\tau, \mathbf{k})T_1^R(\eta, \mathbf{k})], \quad (4.13)$$

$$= \frac{1}{k}\Theta(\tau - \eta)e^{\pi(2m_Q + m_Q^{-1})} \text{Im}[W_{\beta, \alpha}^*(2ik\tau)W_{\beta, \alpha}(2ik\eta)], \quad (4.14)$$

where $\text{Im}(z)$ denotes an imaginary part of a complex number z . Dependence of Green's function on the homogeneous solution also ensures that the second order left-handed polarisation of the gauge field is sub-dominant, even if sourced by the first order right-handed polarisation.

Then, the second order gauge field is given as

$$\begin{aligned} \hat{t}_2^R(\tau, \mathbf{k}) &= ge_{ij}^L(\mathbf{k}) \int_{-\infty}^{\infty} d\eta G_t(\tau, \eta, k) \\ &\quad \times \int \frac{d^3q_1 d^3q_2}{(2\pi)^6} \delta_D(\mathbf{q}_1 + \mathbf{q}_2 - \mathbf{k}) Q_{ij}^{(i)}(\mathbf{q}_1, \mathbf{q}_2, \eta) \hat{t}_1^R(\eta, \mathbf{q}_1) \hat{t}_1^R(\eta, \mathbf{q}_2), \end{aligned} \quad (4.15)$$

which yields the second order sourced metric perturbation (c.f. equation (3.8)) as

$$\hat{\psi}_2^R(\tau, \mathbf{k}) = \int_{-\infty}^{\infty} d\eta G_\psi(\tau, \eta, k) \mathcal{D}(\eta, k) \hat{t}_2^R(\eta, k). \quad (4.16)$$

Substituting $\hat{\psi}_1^R$ and the above expression for $\hat{\psi}_2^R$ into eq. (4.2), we obtain

$$\begin{aligned} &\langle \hat{\psi}_1^R(\tau, \mathbf{k}_1) \hat{\psi}_1^R(\tau, \mathbf{k}_2) \hat{\psi}_2^R(\tau, \mathbf{k}_3) \rangle = \\ &= \int \prod_{i=1}^3 (d\eta_i G_\psi(\tau, \eta_i, k_i) \mathcal{D}(\eta_i, k_i)) \langle \hat{t}_1^R(\eta_1, \mathbf{k}_1) \hat{t}_1^R(\eta_2, \mathbf{k}_2) \hat{t}_2^R(\eta_3, \mathbf{k}_3) \rangle, \\ &= \int \prod_{i=1}^3 (d\eta_i G_\psi(\tau, \eta_i, k_i) \mathcal{D}(\eta_i, k_i)) T_1^R(\eta_1, k_1) T_1^R(\eta_2, k_2) g e_{jl}^L(\mathbf{k}_3) \int d\eta G_t(\eta_3, \eta, k_3) \\ &\quad \times \int \frac{d^3q_1 d^3q_2}{(2\pi)^6} \delta_D(\mathbf{q}_1 + \mathbf{q}_2 - \mathbf{k}_3) Q_{jl}(\mathbf{q}_1, \mathbf{q}_2, \eta_3) T_1^{*R}(\eta, q_1) T_1^{*R}(\eta, q_2) \langle \hat{a}_{\mathbf{k}_1}^R \hat{a}_{\mathbf{k}_2}^R \hat{a}_{-\mathbf{q}_1}^{R\dagger} \hat{a}_{-\mathbf{q}_2}^{R\dagger} \rangle, \\ &= (2\pi)^3 \delta_D(\mathbf{k}_1 + \mathbf{k}_2 + \mathbf{k}_3) g \Psi_1^R(\tau, k_1) \Psi_1^R(\tau, k_2) \int d\eta_3 G_\psi(\tau, \eta_3, k_3) \mathcal{D}(\eta_3, k_3) \\ &\quad \times \int d\eta G_t(\eta_3, \eta, k_3) e_{ij}^L(\mathbf{k}_3) [Q_{ij}(-\mathbf{k}_1, -\mathbf{k}_2, \eta) + Q_{ij}(-\mathbf{k}_2, -\mathbf{k}_1, \eta)] T_1^{*R}(\eta, k_1) T_1^{*R}(\eta, k_2). \end{aligned} \quad (4.17)$$

As discussed in appendix. A, contraction of the polarisation tensors is calculated as

$$e_{ij}^L(\mathbf{k}_3) [Q_{ij}^{(i)}(-\mathbf{k}_1, -\mathbf{k}_2, \eta) + Q_{ij}^{(i)}(-\mathbf{k}_2, -\mathbf{k}_1, \eta)] = -2k_1 \Xi [\tilde{\Xi} + (3m_Q + 2\xi)/\eta], \quad (4.18)$$

where we have defined

$$\tilde{\Xi} = 1 + r_2 + r_3, \quad \Xi = \frac{(1 + r_2 + r_3)^3}{64r_2^2 r_3^2} (r_2 + r_3 - 1)(r_2 - r_3 + 1)(-r_2 + r_3 + 1), \quad (4.19)$$

with $r_2 \equiv k_2/k_1$ and $r_3 = k_3/k_1$. Using this, we obtain

$$\begin{aligned} \left\langle \hat{\psi}_1^R(\tau, \mathbf{k}_1) \hat{\psi}_1^R(\tau, \mathbf{k}_2) \hat{\psi}_2^R(\tau, \mathbf{k}_3) \right\rangle &= (2\pi)^3 \delta_D(\mathbf{k}_1 + \mathbf{k}_2 + \mathbf{k}_3) (-2g\Xi k_1) \Psi_1^R(\tau, k_1) \Psi_1^R(\tau, k_2) \\ &\times \int d\eta_3 G_\psi(\tau, \eta_3, k_3) \mathcal{D}(\eta_3, k_3) \int d\eta G_t(\eta_3, \eta, k_3) \left[\tilde{\Xi} + \frac{(5m_Q + 2m_Q^{-1})}{k_1\eta} \right] T_1^{*R}(\eta, k_1) T_1^{*R}(\eta, k_2). \end{aligned} \quad (4.20)$$

Since we are interested in the bispectrum in the super-horizon limit $k\tau \rightarrow 0$, Green's function $G_\psi(\tau, \eta_3, k_3)$ can be reduced. By changing the integration variables from η_3 and η to $y \equiv -k_1\eta_3$ and $z \equiv -k_1\eta$, we obtain

$$\begin{aligned} &\lim_{|k_3\tau| \rightarrow 0} \int d\eta_3 G_\psi(\tau, \eta_3, k_3) \mathcal{D}(\eta_3, k_3) \int d\eta G_t(\eta_3, \eta, k_3) \left[\tilde{\Xi} + \frac{(3m_Q + 2\xi)}{k_1\eta} \right] T_1^{*R}(\eta, k_1) T_1^{*R}(\eta, k_2) \\ &= \frac{\sqrt{\epsilon_B} e^{2\pi(2m_Q + m_Q^{-1})}}{\sqrt{r_2 r_3^4 k_1^4 \tau}} \int_0^{x_{\max}} \frac{dy}{y^2} \left[r_3 y \cos(r_3 y) - \sin(r_3 y) \right] \left(m_Q^{-1} \partial_y + \frac{m_Q}{y} - r_3 \right) \\ &\times \int_y^{x_{\max}} dz \operatorname{Im} \left[W_{\beta, \alpha}^*(-2ir_3 y) W_{\beta, \alpha}(-2ir_3 z) \right] \left(\tilde{\Xi} - \frac{(5m_Q + 2m_Q^{-1})}{z} \right) W_{\beta, \alpha}^*(-2iz) W_{\beta, \alpha}^*(-2ir_2 z), \\ &\equiv \frac{\sqrt{\epsilon_B} e^{2\pi(2m_Q + m_Q^{-1})}}{\sqrt{r_2 r_3^4 k_1^4 \tau}} \mathcal{N}_3, \end{aligned} \quad (4.21)$$

where we have introduced the UV cutoff $x_{\max} \equiv 2m_Q + m_Q^{-1} + \sqrt{2m_Q^2 + 2 + m_Q^{-2}}$, at which t_1^R starts undergoing a tachyonic instability, to avoid incorporating unphysical vacuum contributions. The integration result is not sensitive to the precise value of the cutoff, as we checked numerically for several different values of x_{\max} . Using the super horizon solution for Ψ_1^R , equation (3.17), and $\psi_{ij} = aM_P h_{ij}/2$ we finally obtain

$$\left\langle \hat{h}_1^R(\tau, \mathbf{k}_1) \hat{h}_1^R(\tau, \mathbf{k}_2) \hat{h}_2^R(\tau, \mathbf{k}_3) \right\rangle = (2\pi)^3 \delta_D(\mathbf{k}_1 + \mathbf{k}_2 + \mathbf{k}_3) \frac{8g\Xi\epsilon_B^{3/2}}{k_1^2 k_2^2 k_3^2} \left(\frac{H}{M_P} \right)^3 r_3^{-2} \mathcal{F}^2 \mathcal{N}_3. \quad (4.22)$$

The factor of $\delta_D(\mathbf{k}_1 + \mathbf{k}_2 + \mathbf{k}_3)$ ensures the triangle condition, namely that the three wave vectors \mathbf{k}_1 , \mathbf{k}_2 , and \mathbf{k}_3 form a closed triangle. This is a consequence of homogeneity and isotropy of the Universe. In the same way, the other two terms in eq. (4.2) can be calculated. Combining them, we obtain the contribution from the diagram (i) as [30],

$$B_h^{(i)}(k_1, k_2, k_3) = \frac{8m_Q^2 \Xi \epsilon_B}{k_1^2 k_2^2 k_3^2} e^{2\pi(2m_Q + m_Q^{-1})} \left(\frac{H}{M_P} \right)^4 \left[\mathcal{F}^{*2} \mathcal{N}_1 + r_2^{-2} |\mathcal{F}|^2 \mathcal{N}_2 + r_3^{-2} \mathcal{F}^2 \mathcal{N}_3 \right], \quad (4.23)$$

with

$$\begin{aligned} \mathcal{N}_i &\equiv \int_0^{x_{\max}} \frac{dy}{y^2} [r_i y \cos(r_i y) - \sin(r_i y)] \left(m_Q^{-1} \partial_y + m_Q y^{-1} - r_i \right) \\ &\times \int_y^{x_{\max}} dz \operatorname{Im} [W_{\beta, \alpha}^*(-2ir_i y) W_{\beta, \alpha}(-2ir_i z)] \left(1 + r_2 + r_3 - \frac{5m_Q + 2m_Q^{-1}}{z} \right) \mathcal{W}_i(z), \end{aligned} \quad (4.24)$$

where $\mathcal{W}_1(z) = W_{\beta, \alpha}(-2ir_2 z) W_{\beta, \alpha}(-2ir_3 z)$, $\mathcal{W}_2(z) = W_{\beta, \alpha}^*(-2iz) W_{\beta, \alpha}(-2ir_3 z)$, and $\mathcal{W}_3(z) = W_{\beta, \alpha}^*(-2ir_2 z) W_{\beta, \alpha}^*(-2iz)$.

Figure 3 shows the tensor bispectrum from the diagram (i). We shall discuss the shape of the bispectrum in detail in section 5.

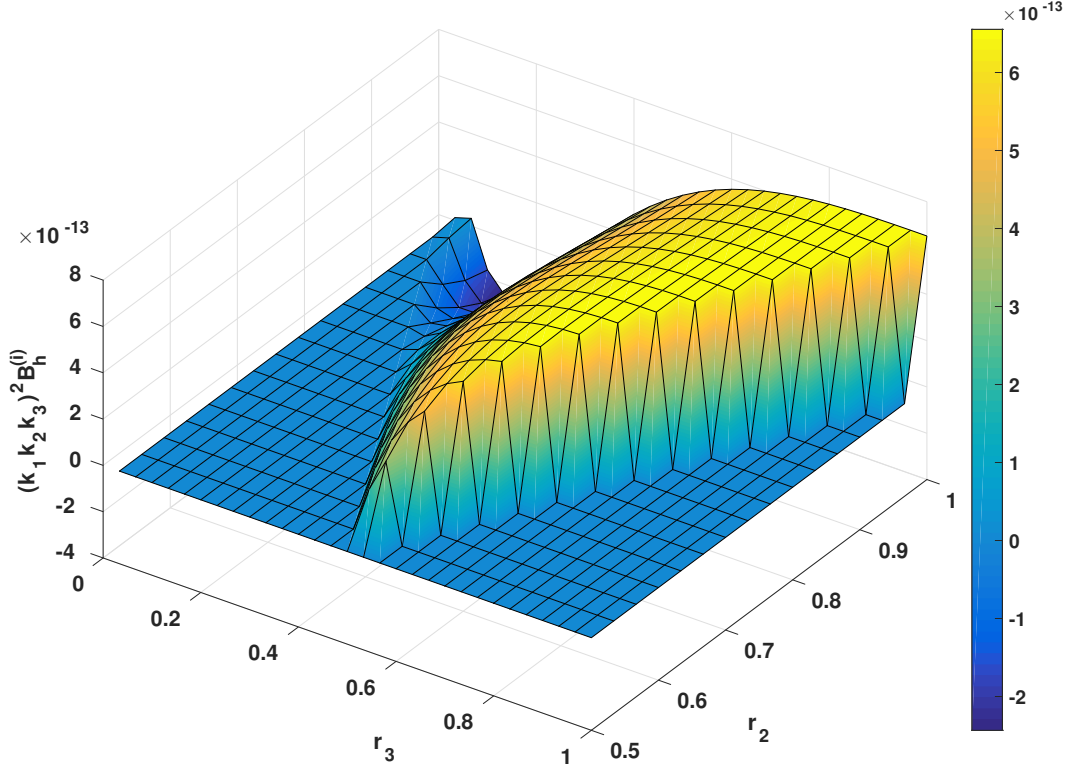


Figure 3: 3D plot of $(k_1 k_2 k_3)^2 B_h^{(i)}$ contributed by the diagram (i). We show only $r_3 \leq r_2$ and the triangle condition implies a bispectrum is non-zero only for $r_2 + r_3 \geq 1$. This shape has a plateau around $0.6 \lesssim r_2 \simeq r_3 \leq 1$. The parameters are $H = 8 \times 10^{12} \text{GeV}$, $m_Q = 3.15$, and $\epsilon_B = 3 \times 10^{-4}$.

4.2 Diagram (ii)

The bispectrum from the diagram (ii) is generated by a non-linear sourcing of the gravitational wave via the $\mathcal{O}(\psi tt)$ terms in the Lagrangian, $L_3^{(ii)}$. The EoM for the second order gravitational wave with the corresponding source terms in Fourier space is given by

$$\left[\partial_\tau^2 + k^2 - \frac{2}{\tau^2} \right] \hat{\psi}_2^R(\tau, \mathbf{k}) = \frac{H}{M_{\text{P}}} [e_{ij}^R(\mathbf{k})]^{-1} S_{ij}^{(ii)}(\tau, \mathbf{k}), \quad (4.25)$$

where the source term is written as the sum of two parts,

$$\begin{aligned} S_{ij}^{(ii)}(\tau, \mathbf{k}) &\equiv \int d^3x e^{-i\mathbf{k}\cdot\mathbf{x}} \frac{\delta L_3^{(ii)}}{\delta \psi_{ij}(\tau, \mathbf{x})}, \\ &= \int \frac{d^3q_1 d^3q_2}{(2\pi)^6} \delta_D(\mathbf{q}_1 + \mathbf{q}_2 - \mathbf{k}) \left[\mathcal{S}_{1ij}^{(ii)}(\tau, \mathbf{q}_1, \mathbf{q}_2) + \mathcal{S}_{2ij}^{(ii)}(\tau, \mathbf{q}_1, \mathbf{q}_2) \right]. \end{aligned} \quad (4.26)$$

$\mathcal{S}_{1ij}^{(ii)}$ has terms without time derivatives,

$$\begin{aligned} \mathcal{S}_{1ij}^{(ii)}(\tau, \mathbf{q}_1, \mathbf{q}_2) &= \left[\frac{3m_Q^2}{\tau} e_{ci}^R(\mathbf{q}_1) e_{cj}^R(\mathbf{q}_2) - 2m_Q \left\{ \epsilon^{acp} e_{pj}^R(\mathbf{q}_1) e_{ai}^R(\mathbf{q}_2) i q_{2c} \right. \right. \\ &\quad \left. \left. + \epsilon^{apj} e_{pc}^R(\mathbf{q}_1) e_{ai}^R(\mathbf{q}_2) i q_{2c} - \epsilon^{apj} e_{pc}^R(\mathbf{q}_1) e_{ac}^R(\mathbf{q}_2) i q_{2i} \right\} + \tau \left\{ e_{ai}^R(\mathbf{q}_1) e_{aj}^R(\mathbf{q}_2) q_{1c} q_{2c} \right. \right. \\ &\quad \left. \left. + e_{ac}^R(\mathbf{q}_1) e_{ac}^R(\mathbf{q}_2) q_{1i} q_{2j} - 2e_{ai}^R(\mathbf{q}_1) e_{ac}^R(\mathbf{q}_2) q_{1c} q_{2j} \right\} \right] \hat{t}_1^R(\tau, \mathbf{q}_1) \hat{t}_1^R(\tau, \mathbf{q}_2) \\ &\equiv Q_{1ij}^{(ii)}(\tau, \mathbf{q}_1, \mathbf{q}_2) \hat{t}_1^R(\tau, \mathbf{q}_1) \hat{t}_1^R(\tau, \mathbf{q}_2), \end{aligned} \quad (4.27)$$

whereas $\mathcal{S}_{2ij}^{(ii)}$ comes from time derivatives of \hat{t}_1^R ,

$$\begin{aligned} \mathcal{S}_{2ij}^{(ii)}(\tau, \mathbf{q}_1, \mathbf{q}_2) &= \tau e_{ai}^R(\mathbf{q}_1) e_{aj}^R(\mathbf{q}_2) \hat{t}_1^R(\tau, \mathbf{q}_1) \hat{t}_1^R(\tau, \mathbf{q}_2) \\ &\equiv Q_{2ij}^{(ii)}(\tau, \mathbf{q}_1, \mathbf{q}_2) \hat{t}_1^R(\tau, \mathbf{q}_1) \hat{t}_1^R(\tau, \mathbf{q}_2). \end{aligned} \quad (4.28)$$

The second order gravitational wave is given using Green's function,

$$\begin{aligned} \hat{\psi}_2^R(\tau, \mathbf{k}) &= \frac{H}{M_{\text{P}}} \int_{-\infty}^{\infty} d\eta G_\psi(\tau, \eta, k) \int \frac{d^3 q_1 d^3 q_2}{(2\pi)^6} \delta_D(\mathbf{q}_1 + \mathbf{q}_2 - \mathbf{k}) \\ &\quad \times e_{ij}^L(\mathbf{k}) \left[Q_{1ij}^{(ii)}(\eta, \mathbf{q}_1, \mathbf{q}_2) \hat{t}_1^R(\eta, \mathbf{q}_1) \hat{t}_1^R(\eta, \mathbf{q}_2) + Q_{2ij}^{(ii)}(\eta, \mathbf{q}_1, \mathbf{q}_2) \hat{t}_1^R(\eta, \mathbf{q}_1) \hat{t}_1^R(\eta, \mathbf{q}_2) \right]. \end{aligned} \quad (4.29)$$

We can now compute the first term in eq. (4.2) produced via the diagram (ii) as

$$\begin{aligned} &\left\langle \hat{\psi}_1^R(\tau, \mathbf{k}_1) \hat{\psi}_1^R(\tau, \mathbf{k}_2) \hat{\psi}_2^R(\tau, \mathbf{k}_3) \right\rangle = \\ &\frac{H}{M_{\text{P}}} \int \prod_{i=1}^2 \left(d\eta_i G_\psi(\tau, \eta_i, k_i) \mathcal{D}(\eta_i, k_i) \right) \int d\eta_3 G_\psi(\tau, \eta_3, k_3) \int \frac{d^3 q_1 d^3 q_2}{(2\pi)^6} \delta_D(\mathbf{q}_1 + \mathbf{q}_2 - \mathbf{k}_3) \\ &\quad \times e_{jl}^L(\mathbf{k}) \left[\left\langle \hat{t}_1^R(\eta_1, \mathbf{k}_1) \hat{t}_1^R(\eta_2, \mathbf{k}_2) \hat{t}_1^R(\eta_3, \mathbf{q}_1) \hat{t}_1^R(\eta_3, \mathbf{q}_2) \right\rangle Q_{1jl}^{(ii)}(\eta_3, \mathbf{q}_1, \mathbf{q}_2) \right. \\ &\quad \left. + \left\langle \hat{t}_1^R(\eta_1, \mathbf{k}_1) \hat{t}_1^R(\eta_2, \mathbf{k}_2) \hat{t}_1^R(\eta_3, \mathbf{q}_1) \hat{t}_1^R(\eta_3, \mathbf{q}_2) \right\rangle Q_{2jl}^{(ii)}(\eta_3, \mathbf{q}_1, \mathbf{q}_2) \right]. \end{aligned} \quad (4.30)$$

The expectation values of the 4-point functions are given by

$$\begin{aligned} &\left\langle \hat{t}_1^R(\eta_1, \mathbf{k}_1) \hat{t}_1^R(\eta_2, \mathbf{k}_2) \hat{t}_1^R(\eta_3, \mathbf{q}_1) \hat{t}_1^R(\eta_3, \mathbf{q}_2) \right\rangle \\ &= (2\pi)^6 (\delta_{\mathbf{k}_1 \mathbf{q}_1} \delta_{\mathbf{k}_2 \mathbf{q}_2} + \delta_{\mathbf{k}_1 \mathbf{q}_2} \delta_{\mathbf{k}_2 \mathbf{q}_1}) T_1^R(\eta_1, k_1) T_1^R(\eta_2, k_2) T_1^{*R}(\eta_3, q_1) T_1^{*R}(\eta_3, q_2), \end{aligned} \quad (4.31)$$

$$\begin{aligned} &\left\langle \hat{t}_1^R(\eta_1, \mathbf{k}_1) \hat{t}_1^R(\eta_2, \mathbf{k}_2) \hat{t}_1^R(\eta_3, \mathbf{q}_1) \hat{t}_1^R(\eta_3, \mathbf{q}_2) \right\rangle \\ &= (2\pi)^6 (\delta_{\mathbf{k}_1 \mathbf{q}_1} \delta_{\mathbf{k}_2 \mathbf{q}_2} + \delta_{\mathbf{k}_1 \mathbf{q}_2} \delta_{\mathbf{k}_2 \mathbf{q}_1}) T_1^R(\eta_1, k_1) T_1^R(\eta_2, k_2) T_1'^{*R}(\eta_3, q_1) T_1'^{*R}(\eta_3, q_2), \end{aligned} \quad (4.32)$$

where $\delta_{\mathbf{k}_1 \mathbf{q}_1} \equiv \delta_D(\mathbf{k}_1 + \mathbf{q}_1)$. Note that these functions are invariant under interchange of $q_1 \leftrightarrow q_2$. As a result, upon integrating the Dirac delta functions, the polarisation factors in equation (4.30) yield

$$e_{ij}^L(\mathbf{k}_3) \left[Q_{1ij}^{(ii)}(\eta_3, -\mathbf{k}_1, -\mathbf{k}_2) + Q_{1ij}^{(ii)}(\eta_3, -\mathbf{k}_2, -\mathbf{k}_1) \right] = 2\Xi \left[\frac{3m_Q^2}{\eta_3} + k_1^2 r_2 \eta_3 + m_Q k_1 (1 + r_2) \right], \quad (4.33)$$

$$e_{ij}^L(\mathbf{k}_3) \left[Q_{2ij}^{(ii)}(\eta_3, -\mathbf{k}_1, -\mathbf{k}_2) + Q_{2ij}^{(ii)}(\eta_3, -\mathbf{k}_2, -\mathbf{k}_1) \right] = 2\Xi \eta_3, \quad (4.34)$$

where $\Xi \equiv \Xi(r_2, r_3)$ has been defined in equation (4.19). Substituting this in equation (4.30), we obtain

$$\begin{aligned} \left\langle \hat{\psi}_1^R(\tau, \mathbf{k}_1) \hat{\psi}_1^R(\tau, \mathbf{k}_2) \hat{\psi}_2^R(\tau, \mathbf{k}_3) \right\rangle &= (2\pi)^3 \delta_D(\mathbf{k}_1 + \mathbf{k}_2 + \mathbf{k}_3) \\ &\times 2\Xi \Psi_1^R(\tau, \mathbf{k}_1) \Psi_1^R(\tau, \mathbf{k}_2) \frac{H}{M_{\text{P}}} \int d\eta_3 G_\psi(\tau, \eta_3, k_3) \left[\eta_3 T_1'^{*R}(\eta_3, k_1) T_1'^{*R}(\eta_3, k_2) \right. \\ &\quad \left. + \left\{ r_2 k_1^2 \eta_3 + m_Q k_1 (1 + r_2) + \frac{3m_Q^2}{\eta_3} \right\} T_1^{*R}(\eta_3, k_1) T_1^{*R}(\eta_3, k_2) \right]. \end{aligned} \quad (4.35)$$

We can similarly evaluate the other two terms in eq. (4.2) contributed from $L_3^{(ii)}$. Taking the super-horizon limit, we obtain [30],

$$k_1^2 k_2^2 k_3^2 B_h^{(ii)}(k_1, k_2, k_3) = 4\Xi \epsilon_B e^{\pi(2m_Q + m_Q^{-1})} \left(\frac{H}{M_{\text{Pl}}} \right)^4 \left[\mathcal{F}^{*2} \tilde{\mathcal{N}}_1 + r_2^{-1} |\mathcal{F}|^2 \tilde{\mathcal{N}}_2 + r_3^{-1} \mathcal{F}^2 \tilde{\mathcal{N}}_3 \right], \quad (4.36)$$

with

$$\begin{aligned} \tilde{\mathcal{N}}_i &\equiv \int_0^{x_{\text{max}}} \frac{dy}{y} [r_i y \cos(r_i y) - \sin(r_i y)] [y \tilde{\mathcal{W}}_i(y) \\ &\quad + \left(\frac{r_1 r_2 r_3}{r_i} y - (r_1 + r_2 + r_3 - r_i) m_Q + \frac{3m_Q^2}{y} \right) \mathcal{W}_i(y)], \end{aligned} \quad (4.37)$$

where $\tilde{\mathcal{W}}_1(y) = \partial_y W_{\beta, \alpha}(-2ir_2 y) \partial_y W_{\beta, \alpha}(-2ir_3 y)$, $\tilde{\mathcal{W}}_2(y) = \partial_y W_{\beta, \alpha}^*(-2iy) \partial_y W_{\beta, \alpha}(-2ir_3 y)$, $\tilde{\mathcal{W}}_3(y) = \partial_y W_{\beta, \alpha}^*(-2ir_2 y) \partial_y W_{\beta, \alpha}^*(-2iy)$, and as before, we have introduced $y \equiv -k_1 \tau$.

Figure 4 shows the gravitational wave bispectrum from the diagram (ii). The magnitude of this bispectrum is smaller than that of the diagram (i) by a factor of a few for this choice of parameters (however, see section 4.4 for more details on the relative amplitudes and shape of the bispectrum), and they have the opposite signs. The bispectrum from the diagram (ii) peaks in the equilateral configuration, $r_2 = r_3 = 1$.

4.3 Diagram (iii)

For the diagram (iii), we consider the second order gravitational wave $\hat{\psi}_2^R$ sourced by a first order gauge field perturbation \hat{t}_1^R and a first order metric perturbation $\hat{\psi}_1^R$. The EoM for $\hat{\psi}_2^R$ is derived from $L_3^{(iii)}$ to be,

$$\left[\partial_\tau^2 + k^2 - \frac{2}{\tau^2} \right] \hat{\psi}_2^R(\tau, \mathbf{k}) = \frac{H}{M_{\text{P}}} [e_{ij}^R(\mathbf{k})]^{-1} \mathcal{S}_{ij}^{(iii)}(\tau, \mathbf{k}), \quad (4.38)$$

where the source term is again written as the sum of two parts,

$$\begin{aligned} \mathcal{S}_{ij}^{(iii)}(\tau, \mathbf{k}) &\equiv \int d^3x e^{-i\mathbf{k}\cdot\mathbf{x}} \frac{\delta L_3^{(iii)}}{\delta \psi_{ij}(\tau, \mathbf{x})}, \\ &= \int \frac{d^3q_1 d^3q_2}{(2\pi)^6} \delta_D(\mathbf{q}_1 + \mathbf{q}_2 - \mathbf{k}) 4\sqrt{\epsilon_B} \left[\mathcal{S}_{1ij}^{(iii)}(\tau, \mathbf{q}_1, \mathbf{q}_2) + \mathcal{S}_{2ij}^{(iii)}(\tau, \mathbf{q}_1, \mathbf{q}_2) \right]. \end{aligned} \quad (4.39)$$

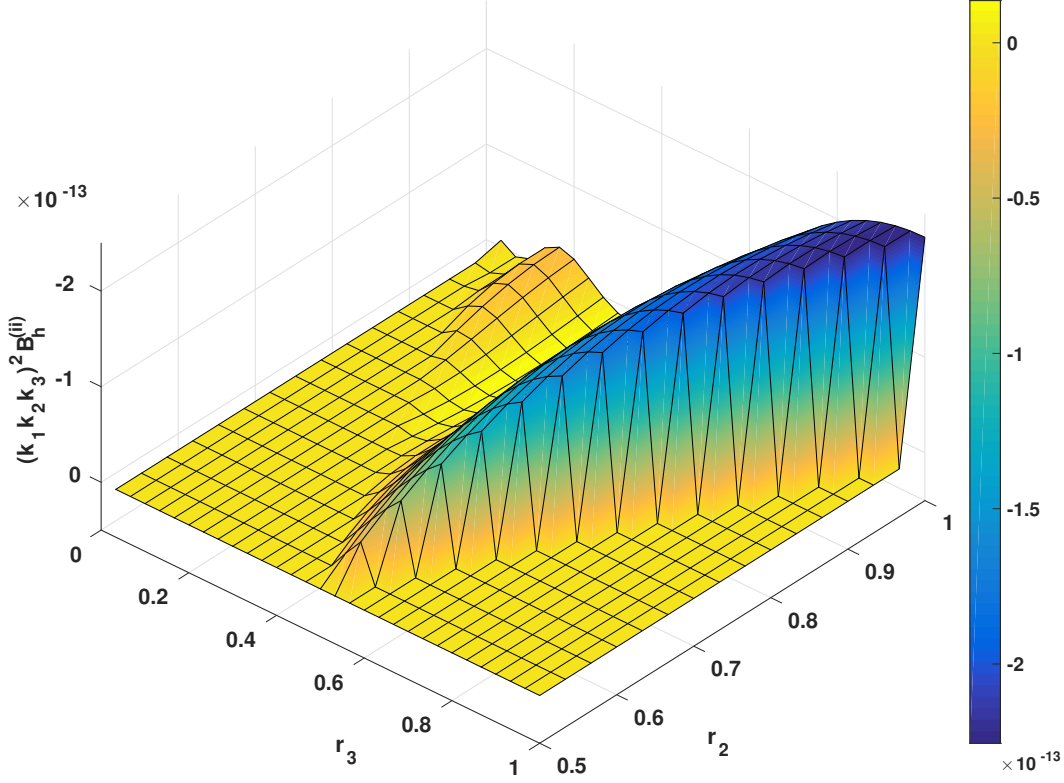


Figure 4: 3D plot of $(k_1 k_2 k_3)^2 B_h^{(ii)}$ for diagram 2. Note that the z -axis has been reversed to show negative values. As before, the parameters are $H = 8 \times 10^{12} \text{GeV}$, $m_Q = 3.15$, and $\epsilon_B = 3 \times 10^{-4}$.

The first part depends on the fields without time derivatives,

$$\mathcal{S}_{1ij}^{(iii)}(\tau, \mathbf{q}_1, \mathbf{q}_2) = -\hat{t}_1^R(\tau, \mathbf{q}_1) \hat{\psi}_1^R(\tau, \mathbf{q}_2) \left[2 |\mathbf{q}_1| e_{ai}^R(\mathbf{q}_1) e_{aj}^R(\mathbf{q}_2) + i \epsilon^{apj} e_{ai}^R(\mathbf{q}_1) e_{lp}^R(\mathbf{q}_2) q_{1l} + i \epsilon^{ajp} e_{al}^R(\mathbf{q}_1) e_{lp}^R(\mathbf{q}_2) q_{1i} \right], \quad (4.40)$$

whereas the second part includes time derivatives of the gauge field perturbation,

$$\mathcal{S}_{2ij}^{(iii)}(\tau, \mathbf{q}_1, \mathbf{q}_2) = m_Q^{-1} e_{ai}^R(\mathbf{q}_1) e_{aj}^R(\mathbf{q}_2) \hat{t}_1^R(\tau, \mathbf{q}_1) \hat{\psi}_1^R(\tau, \mathbf{q}_2). \quad (4.41)$$

However, we find that the first part multiplied by the polarisation factor vanishes: $e_{ij}^L(\mathbf{k}_3) \mathcal{S}_{1ij}^{(iii)}(\tau, -\mathbf{k}_1, -\mathbf{k}_2) = 0$, for all the permutations of \mathbf{k}_1 , \mathbf{k}_2 , and \mathbf{k}_3 . Hence we consider only the second part. With Green's function, we find the second order gravitational wave as

$$\hat{\psi}_2^R(\tau, \mathbf{k}) = \frac{4\sqrt{\epsilon_B}}{m_Q} \frac{H}{M_{\text{P}}} \int_{-\infty}^{\infty} d\eta G_\psi(\tau, \eta, k) \int \frac{d^3 q_1 d^3 q_2}{(2\pi)^6} \delta_D(\mathbf{q}_1 + \mathbf{q}_2 - \mathbf{k}) \times \left[\hat{t}_1^R(\eta, \mathbf{q}_1) \hat{\psi}_1^R(\eta, \mathbf{q}_2) e_{ij}^L(\mathbf{k}) e_{ia}^R(\mathbf{q}_1) e_{aj}^R(\mathbf{q}_2) \right]. \quad (4.42)$$

The first term in eq. (4.2) from the diagram (iii) yields

$$\begin{aligned} \langle \hat{\psi}_1^R(\tau, \mathbf{k}_1) \hat{\psi}_1^R(\tau, \mathbf{k}_2) \hat{\psi}_2^R(\tau, \mathbf{k}_3) \rangle &= \frac{4\sqrt{\epsilon_B}}{m_Q} \frac{H}{M_P} \int \prod_{i=1}^2 (d\eta_i G_\psi(\tau, \eta_i, k_i) \mathcal{D}(\eta_i, k_i)) \int d\eta_3 G_\psi(\tau, \eta_3, k_3) \\ &\times \int \frac{d^3 q_1 d^3 q_2}{(2\pi)^6} \delta_D(\mathbf{q}_1 + \mathbf{q}_2 - \mathbf{k}_3) \langle \hat{t}_1^R(\eta_1, \mathbf{k}_1) \hat{t}_1^R(\eta_2, \mathbf{k}_2) \hat{t}_1^R(\eta_3, \mathbf{q}_1) \hat{\psi}_1^R(\eta_3, \mathbf{q}_2) \rangle e_{jl}^L(\mathbf{k}_3) e_{ja}^R(\mathbf{q}_1) e_{al}^R(\mathbf{q}_2). \end{aligned} \quad (4.43)$$

The expectation value is calculated as

$$\begin{aligned} \langle \hat{t}_1^R(\eta_1, \mathbf{k}_1) \hat{t}_1^R(\eta_2, \mathbf{k}_2) \hat{t}_1^R(\eta_3, \mathbf{q}_1) \hat{\psi}_1^R(\eta_3, \mathbf{q}_2) \rangle &= (2\pi)^6 (\delta_{\mathbf{k}_1 \mathbf{q}_1} \delta_{\mathbf{k}_2 \mathbf{q}_2} + \delta_{\mathbf{k}_1 \mathbf{q}_2} \delta_{\mathbf{k}_2 \mathbf{q}_1}) \\ &\times T_1^R(\eta_1, k_1) T_1^R(\eta_2, k_2) T_1'^* R(\eta_3, q_1) \Psi_1^* R(\eta_3, q_2). \end{aligned} \quad (4.44)$$

Then, equation (4.43) reads

$$\begin{aligned} \langle \hat{\psi}_1^R(\tau, \mathbf{k}_1) \hat{\psi}_1^R(\tau, \mathbf{k}_2) \hat{\psi}_2^R(\tau, \mathbf{k}_3) \rangle &= (2\pi)^3 \delta_D(\mathbf{k}_1 + \mathbf{k}_2 + \mathbf{k}_3) \Psi_1^R(\tau, k_1) \Psi_1^R(\tau, k_2) \\ &\frac{4\sqrt{\epsilon_B \Xi}}{m_Q} \frac{H}{M_P} \int d\eta_3 G_\psi(\tau, \eta_3, k_3) \left[T_1'^* R(\eta_3, k_1) \Psi_1^* R(\eta_3, k_2) + T_1'^* R(\eta_3, k_2) \Psi_1^* R(\eta_3, k_1) \right]. \end{aligned} \quad (4.45)$$

Combining with the other two terms in eq. (4.2), we obtain the bispectrum from the diagram (iii) as

$$k_1^2 k_2^2 k_3^2 B_h^{(iii)}(k_1, k_2, k_3) = 16\Xi \frac{\epsilon_B^2}{m_Q} e^{\pi(2m_Q + m_Q^{-1})} \left(\frac{H}{M_{\text{Pl}}} \right)^4 \left[\mathcal{F}^{*2} \check{\mathcal{N}}_1 + r_2^{-1} |\mathcal{F}|^2 \check{\mathcal{N}}_2 + r_3^{-1} \mathcal{F}^2 \check{\mathcal{N}}_3 \right], \quad (4.46)$$

with

$$\check{\mathcal{N}}_i \equiv \int_0^{x_{\text{max}}} \frac{dy}{y} [r_i y \cos(r_i y) - \sin(r_i y)] \check{\mathcal{W}}_i(y), \quad (4.47)$$

where we define $\check{\mathcal{W}}_1(y) = \partial_y W_{\beta, \alpha}(-2ir_2 y) \Phi(-2ir_3 y) + \partial_y W_{\beta, \alpha}(-2ir_3 y) \Phi(-2ir_2 y)$, $\check{\mathcal{W}}_2(y) = \partial_y W_{\beta, \alpha}^*(-2iy) \Phi(-2ir_3 y) + \partial_y W_{\beta, \alpha}^*(-2ir_3 y) \Phi(-2iy)$, $\check{\mathcal{W}}_3(y) = \partial_y W_{\beta, \alpha}^*(-2iy) \Phi^*(-2ir_2 y) + \partial_y W_{\beta, \alpha}^*(-2ir_2 y) \Phi^*(-2iy)$, $y \equiv -k_1 \tau$, and

$$\begin{aligned} \Phi(-2ir_i y) &\equiv \frac{1}{r_i y} \int_{r_i y}^{x_{\text{max}}} \frac{dz}{z} [(z - r_i y) \cos(z - r_i y) - (1 + zr_i y) \sin(z - r_i y)] \\ &\times \left[\frac{\partial_z}{m_Q z} + \frac{m_Q - z}{z^2} \right] W_{\beta, \alpha}(-2iz). \end{aligned} \quad (4.48)$$

Figure 5 shows the momentum dependence of the bispectrum from the diagram (iii). We find that the contribution from the diagram (iii) is almost 7 orders of magnitude smaller than that of the diagram (i) and (ii), justifying that we neglected its contribution in our previous work [30]. This diagram is also zero in the folded limit and the bispectrum peaks in the equilateral configuration. The contribution from this diagram is so small that we do not compare the templates to it.

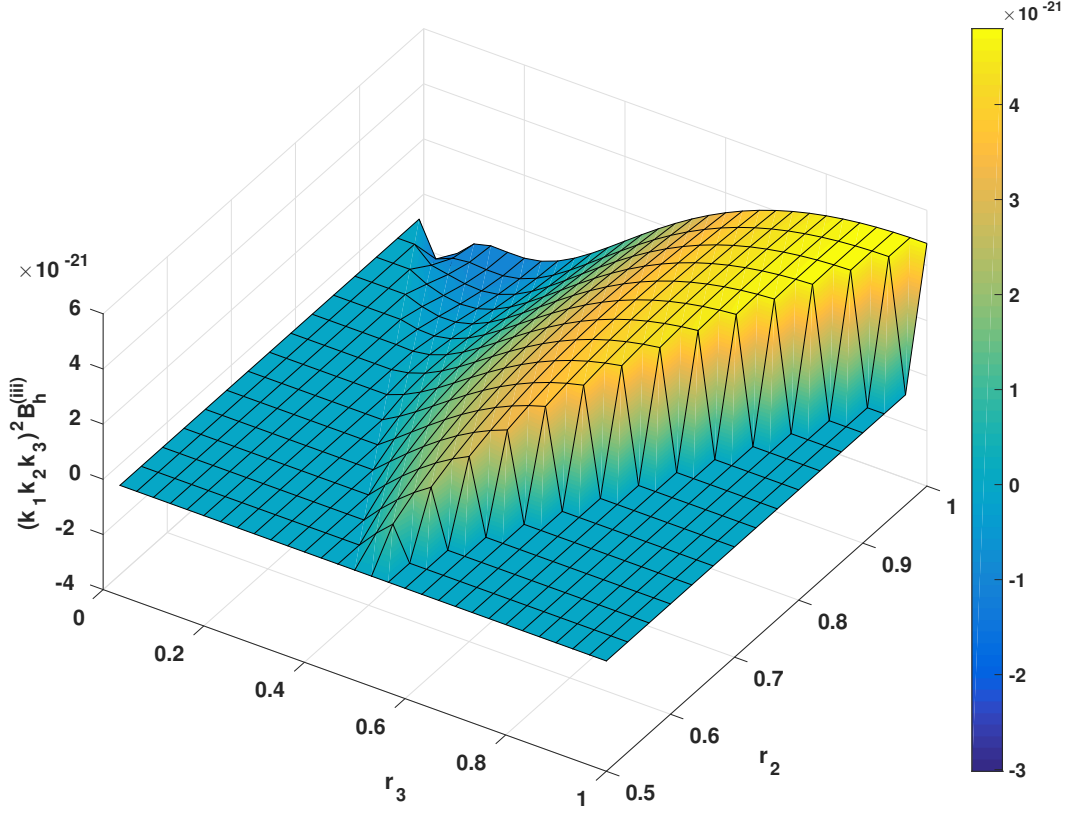


Figure 5: 3D plot of $(k_1 k_2 k_3)^2 B_h^{(iii)}$ for diagram 3. Its magnitude is much smaller than the other two contributions, $B_h^{(i)}$ and $B_h^{(ii)}$, shown in figures 3 and 4, respectively. The parameters are $H = 8 \times 10^{12} \text{GeV}$, $m_Q = 3.15$, and $\epsilon_B = 3 \times 10^{-4}$.

4.4 Total bispectrum

Combining the three contributions which we have calculated in the previous subsections, eqs. (4.23), (4.36) and (4.46), we obtain the total bispectrum of the sourced GWs in our model as

$$\begin{aligned}
 B_h^{RRR}(k_1, k_2, k_3) &= B_h^{(i)} + B_h^{(ii)} + B_h^{(iii)}, \\
 &= \frac{\epsilon_B \Xi(r_2, r_3)}{k_1^2 k_2^2 k_3^2} \left(\frac{H}{M_{\text{P}}} \right)^4 \Upsilon(m_Q, r_2, r_3),
 \end{aligned} \tag{4.49}$$

with

$$\begin{aligned}
 \Upsilon(m_Q, r_2, r_3) &\equiv 8m_Q^2 e^{2\pi(2m_Q + m_Q^{-1})} \left[\mathcal{F}^{*2} \mathcal{N}_1 + r_2^{-2} |\mathcal{F}|^2 \mathcal{N}_2 + r_3^{-2} \mathcal{F}^2 \mathcal{N}_3 \right] \\
 &\quad + 4e^{\pi(2m_Q + m_Q^{-1})} \left[\mathcal{F}^{*2} \tilde{\mathcal{N}}_1 + r_2^{-1} |\mathcal{F}|^2 \tilde{\mathcal{N}}_2 + r_3^{-1} \mathcal{F}^2 \tilde{\mathcal{N}}_3 \right] \\
 &\quad + 16 \frac{\epsilon_B}{m_Q} e^{\pi(2m_Q + m_Q^{-1})} \left[\mathcal{F}^{*2} \check{\mathcal{N}}_1 + r_2^{-1} |\mathcal{F}|^2 \check{\mathcal{N}}_2 + r_3^{-1} \mathcal{F}^2 \check{\mathcal{N}}_3 \right].
 \end{aligned} \tag{4.50}$$

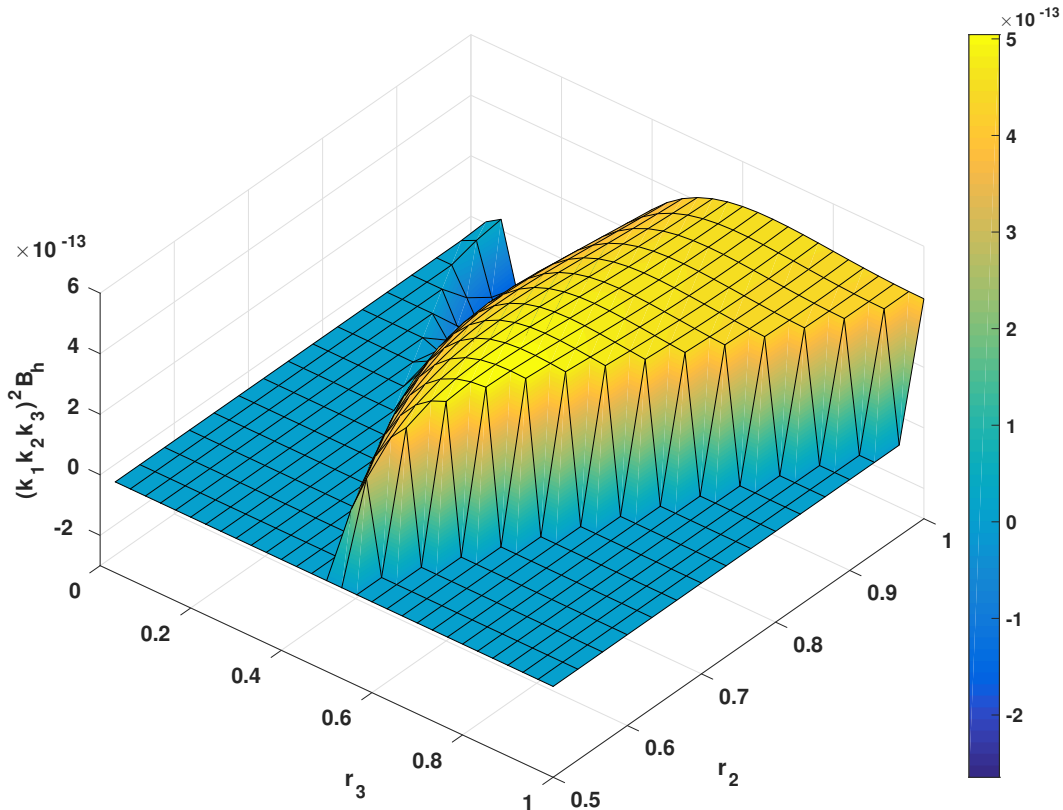


Figure 6: 3D plot of the total bispectrum $(k_1 k_2 k_3)^2 B_h^{RRR}$ given in eq. (4.49). It has a peak at $r_2 \simeq r_3 \approx 0.6$ where the brightest yellow is seen. The parameters are $H = 8 \times 10^{12} \text{ GeV}$, $m_Q = 3.15$, and $\epsilon_B = 3 \times 10^{-4}$.

The ϵ_B dependence of Υ is weak, since the third line in eq.(4.50) from the diagram (iii) is negligible compared to the others. In figure 6, we show the shape of the total bispectrum $(k_1 k_2 k_3)^2 B_h^{RRR}(k_1, k_2, k_3)$. We find a mild peak around $r_2 \simeq r_3 \approx 0.6$ as a result of the combination of the plateau of $B_h^{(i)}$ and the negative slope of $B_h^{(ii)}$ on the $r_2 = r_3$ plane.

Aside from some interesting local features, the shape of our bispectrum B_h^{RRR} looks similar to the equilateral shape shown in figure 15. To quantitatively measure similarity, we calculate the “cosine” between the shape of our bispectrum and the equilateral shape, $\cos(B_h \cdot F_{\text{eq}})$ [40]. Definition of the cosine is described in appendix B. In figure 7, the cosine is shown as a function of m_Q . Note that the cosine depends only on m_Q , because H and ϵ_B change only the overall amplitude as long as the diagram (iii) is negligible. We find that the cosine rises from about 0.5 for $m_Q \sim 2$ to around 0.9 for $m_Q \gtrsim 2.5$ and it varies up to 1% for the parameter range of interest (see section 6). This is because for values of $m_Q < 2.5$ the total bispectrum receives significant negative contribution from the second diagram close to the equilateral limit, thus suppressing the total bispectrum relative to the peak in this region. As a result, the shape becomes quite different from the equilateral shape.

Around 90% similarity to the equilateral shape implies that our gravitational wave

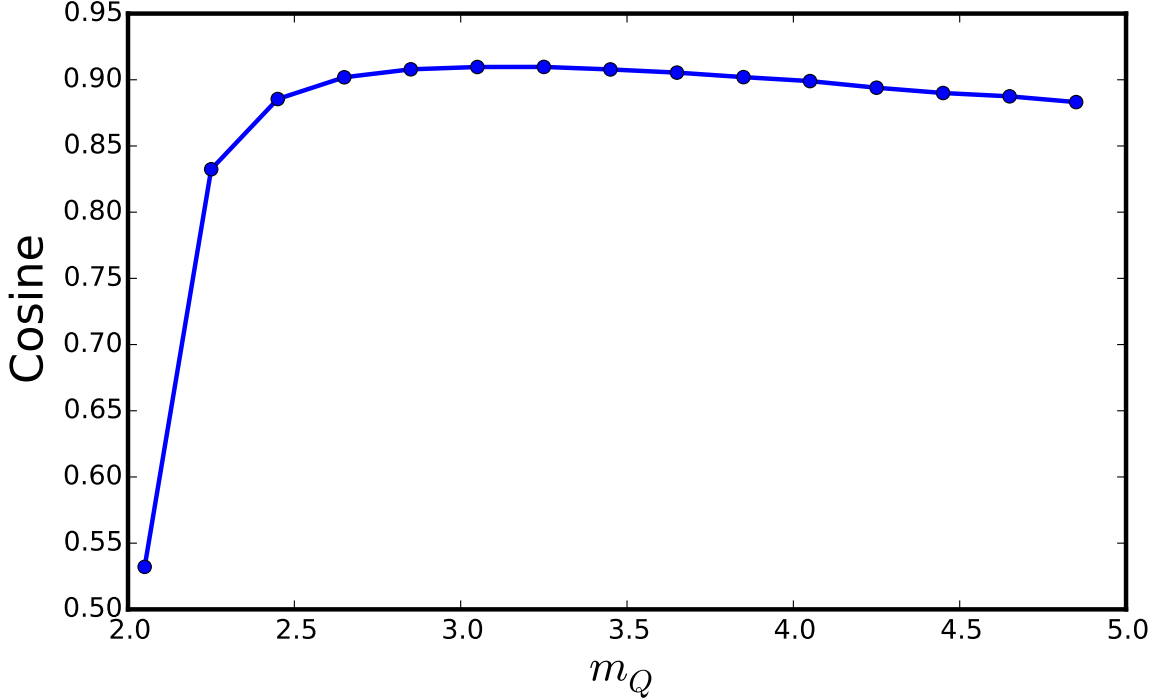


Figure 7: Similarity of the shapes of an equilateral bispectrum and our tensor bispectrum B_h^{RRR} , eq. (4.49), which is calculated as the “cosine” (see appendix B for definition).

bispectrum is reasonably characterized by the amplitude at the equilateral limit, $r_2 = r_3 = 1$. In the equilateral limit, the factors in the bispectrum become

$$\Xi(r_2 = r_3 = 1) = \frac{27}{64} \quad (4.51)$$

and

$$\begin{aligned} \Upsilon_{\text{eq}}(m_Q) &\equiv \Upsilon(m_Q, 1, 1) \\ &\simeq 8m_Q^2 e^{2\pi(2m_Q + m_Q^{-1})} \left[|\mathcal{F}|^2 \mathcal{N}_2 + 2 \text{Re}[\mathcal{F}^2 \mathcal{N}_3] \right] \\ &\quad + 4e^{\pi(2m_Q + m_Q^{-1})} \left[|\mathcal{F}|^2 \tilde{\mathcal{N}}_2 + 2 \text{Re}[\mathcal{F}^2 \tilde{\mathcal{N}}_3] \right], \end{aligned} \quad (4.52)$$

where $\text{Re}[z]$ denotes a real part of a complex number z , and the small contribution from the diagram (iii) is ignored. In figure 8, we plot Υ_{eq} . For $3 \lesssim m_Q \lesssim 5$, Υ_{eq} is well approximated by the following expression:

$$\Upsilon_{\text{eq}} \simeq \exp[0.1377m_Q^3 - 2.128m_Q^2 + 18.96m_Q - 12.8], \quad (2.8 \leq m_Q \leq 4.8). \quad (4.53)$$

Here, the relative error of this fitting formula is less than 1%.

The ratio of the bispectrum to the squared power spectrum of GWs from the vacuum fluctuation of the metric, $B_h^{\text{vac}} / (P_h^{\text{vac}})^2$, is of order unity [31, 32]. The ratio for the sourced GWs can be much greater than unity. From eqs. (3.18) and (4.49), the ratio in the equilateral limit is given by

$$\frac{B_h^{\text{sourced}}(k, k, k)}{(P_h^{\text{sourced}}(k))^2} = \frac{3^3 \Upsilon_{\text{eq}}(m_Q)}{2^8 |\mathcal{F}(m_Q)|^4} \epsilon_B^{-1}. \quad (4.54)$$

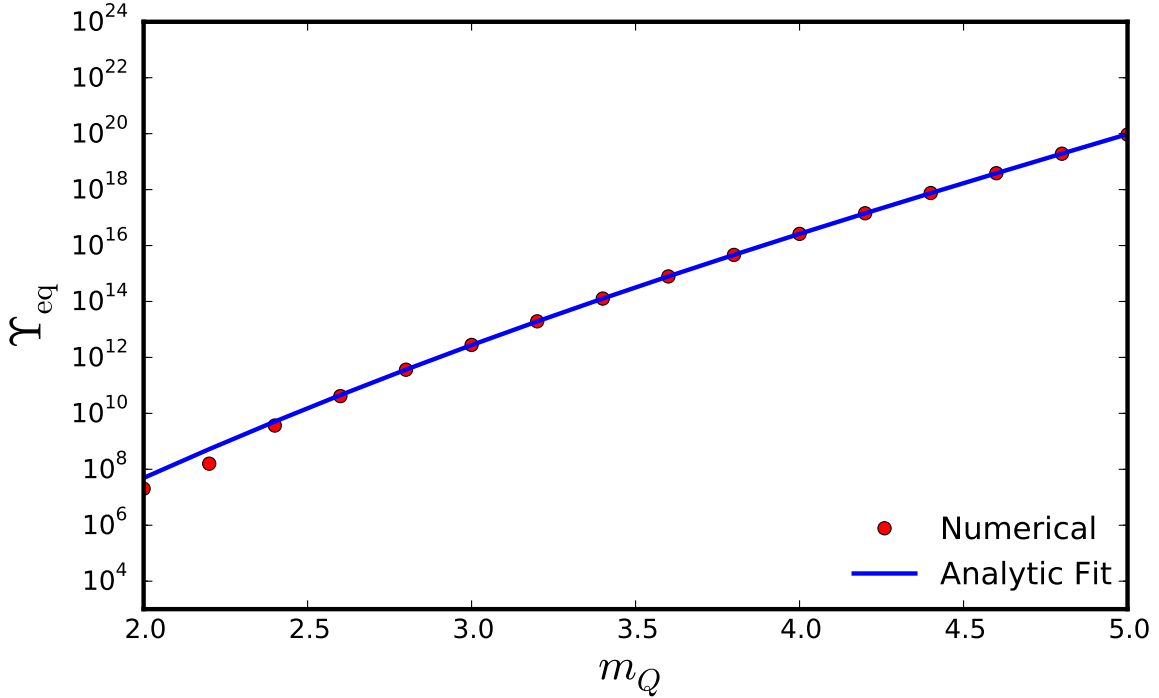


Figure 8: $\Upsilon_{\text{eq}}(m_Q)$ defined in eq. (4.52) and its fitting formula (eq. (4.53)) are plotted as the red dots and blue line, respectively.

In figure 9, we plot $\epsilon_B B_h^{\text{sourced}} / (P_h^{\text{sourced}})^2$ in which steep exponential dependence of the bispectrum and power spectrum on m_Q cancels out, though milder exponential dependence remains. We find a simple relation for a specific range of m_Q ; for instance,

$$\frac{B_h^{\text{sourced}}(k, k, k)}{(P_h^{\text{sourced}}(k))^2} \approx \frac{1.816 e^{0.841 m_Q}}{\epsilon_B} \simeq \frac{0.908 e^{0.841 m_Q}}{\Omega_A}, \quad (3 \lesssim m_Q \lesssim 5), \quad (4.55)$$

where $\Omega_A \equiv (\epsilon_B + \epsilon_E)/2 \simeq (1 + m_Q^{-2})\epsilon_B/2$ (see eq. (2.10)) is the energy density fraction of the background $SU(2)$ gauge field. Note also, that there is a “kink” in the bispectrum at $m_Q \sim 2.25$. This corresponds to the value of m_Q for which the bispectrum from the second diagram is larger in magnitude than diagram one at the equilateral configuration, because of which the total bispectrum becomes negative. Since we plot the absolute value of the bispectrum, this appears as a “kink” in figure 9.

Dependence on the energy density fraction of the gauge fields in eq. (4.55) is analogous to the curvaton mechanism [36, 37], where a similar relation holds for the scalar non-Gaussianity parameter, $f_{\text{NL}} \sim \Omega_\sigma^{-1}$. Ω_σ is the energy density fraction of the curvaton field at its decay time. Therefore the origin of the dependence in eq. (4.55) may be understood in a similar way as the curvaton case [41]: suppose that the metric perturbation h is given by $h = c_1 t$ where t is the mode function of the gauge field. At the same time, t is expanded as $t = t^{(1)} + t^{(2)} + \mathcal{O}(t^{(3)})$ such that $t^{(2)} = c_2 (t^{(1)})^2$. Then $B_h/P_h^2 \sim c_2/c_1$. From equations (3.2) and (3.5), we see that $c_1 \propto \sqrt{\epsilon_B H}/M_{\text{P}}$. We also see from equation (4.9) that $c_2 \propto g$. Thus $B_h/P_h^2 \sim g M_{\text{P}} / (\sqrt{\epsilon_B H}) = m_Q^2/\epsilon_B$. It should be noted, however, that this relation only holds when the gauge field has the dominant contribution to both the tensor power spectrum and bispectrum, and thus, is not valid in the limit $\epsilon_B \rightarrow 0$.

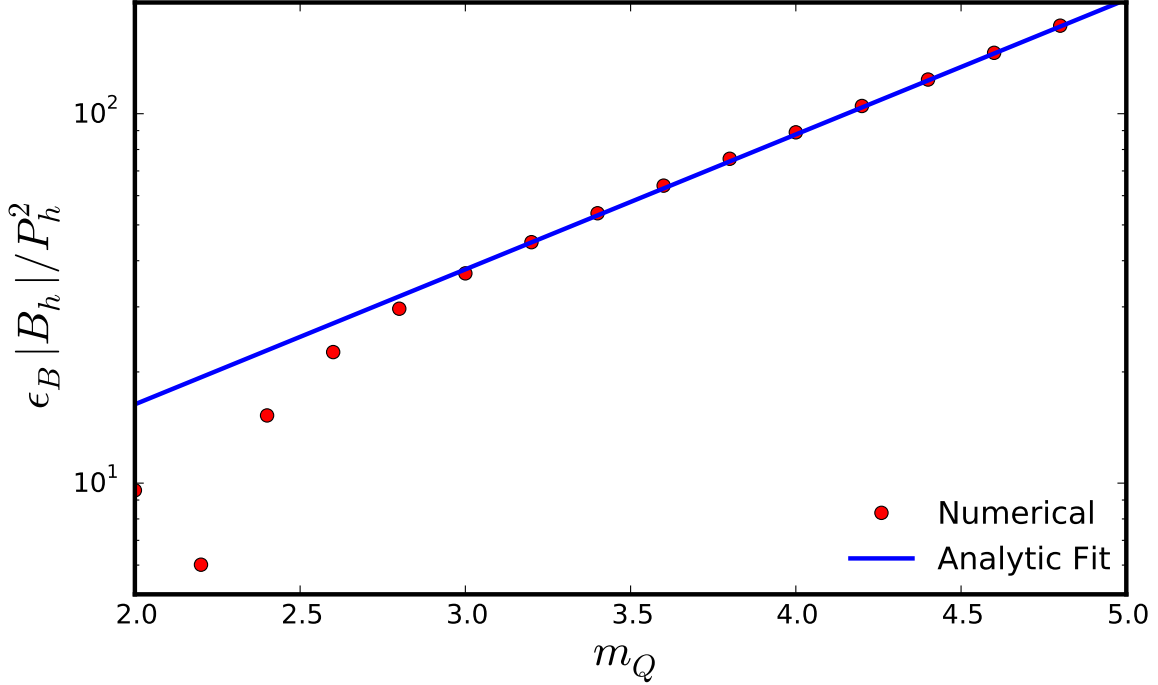


Figure 9: Ratio of the absolute value of the sourced tensor bispectrum to the sourced tensor power spectrum squared (normalised by ϵ_B) as a function of the parameter m_Q , along with its fitting formula (eq. (4.55)), plotted as the red dots and blue line respectively. It rises exponentially as m_Q increases. Since the y -axis shows the ratio normalised by the energy density fraction of the gauge field, ϵ_B , the ratio of the correlation functions can be very large for allowed values of ϵ_B .

5 Peak of Bispectrum

The total tensor bispectrum given in eq. (4.49) has a peak not at the equilateral limit $r_2 = r_3 = 1$ but at $r_2 = r_3 \approx 0.6$ (see figure. 6). In this section, we study why this happens, by looking into the evolution of the tensor perturbations of the $SU(2)$ gauge field t_{ij} .

The shape of the tensor bispectrum is determined by $\mathcal{N}_i(m_Q, r_2, r_3)$ and $\tilde{\mathcal{N}}_i(m_Q, r_2, r_3)$ ($i = 1, 2, 3$) as well as $\Xi(r_2, r_3)$ in eq. (4.49), while the contributions from $\tilde{\mathcal{N}}_i(m_Q, r_2, r_3)$ are negligible. For our current purpose, it suffices to focus on the case with $r_2 = r_3$ in which the three momenta, $\mathbf{k}_1, \mathbf{k}_2, \mathbf{k}_3$, form an obtuse-angled isosceles triangle. In other words, we concentrate on a cross-section surface of the 3D plot, figure 6. For $r \equiv r_2 = r_3$, the r dependence of $\mathcal{N}_i(m_Q, r)$ and $\tilde{\mathcal{N}}_i(m_Q, r)$ is shown in figure 10. We do not plot $|\mathcal{N}_3|$ and $|\tilde{\mathcal{N}}_3|$ which are the same as $|\mathcal{N}_2|$ and $|\tilde{\mathcal{N}}_2|$ for $r_2 = r_3$, respectively. We find that only \mathcal{N}_1 grows significantly as r decreases, while the others have moderate dependences. To understand its behaviour, we look closely at the second line of \mathcal{N}_1 in eq. (4.24) for $r_2 = r_3$,

$$\mathcal{I}_1(m_Q, r, y) \equiv \int_y^{x_{\max}} \frac{dz}{z} \text{Im}[W_{\beta, \alpha}^*(-2iy)W_{\beta, \alpha}(-2iz)] \left(z(1+2r) - 5m_Q - 2m_Q^{-1} \right) \mathcal{W}_1(z). \quad (5.1)$$

In the integrand of \mathcal{I}_1 , the first part, $\text{Im}[W_{\beta, \alpha}^*(-2iy)W_{\beta, \alpha}(-2iz)]$, represents Green's function for t_2^R given in eq. (4.14), and the second part, $\left(z(1+2r) - 5m_Q - 2m_Q^{-1} \right) \mathcal{W}_1(z)$, represents

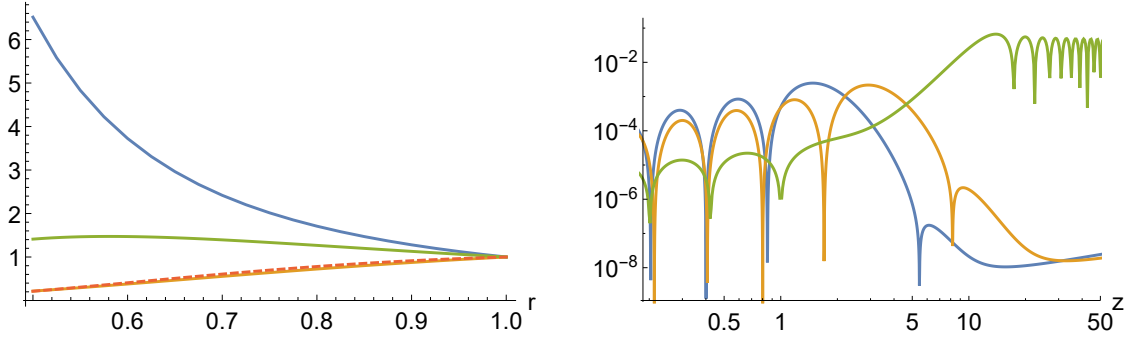


Figure 10: **(Left panel)** Absolute values of \mathcal{N}_i and $\tilde{\mathcal{N}}_i$ normalized by their values at $r = 1$ are shown, namely $|\mathcal{N}_1(r)|/|\mathcal{N}_1(r = 1)|$ (blue), $r^{-2}|\mathcal{N}_2(r)|/|\mathcal{N}_2(r = 1)|$ (orange), $|\tilde{\mathcal{N}}_1(r)|/|\tilde{\mathcal{N}}_1(r = 1)|$ (green) and $r^{-1}|\tilde{\mathcal{N}}_2(r)|/|\tilde{\mathcal{N}}_2(r = 1)|$ (red dashed). **(Right panel)** Absolute value of the source term part in the integrand of \mathcal{I}_1 , namely $|(z(1 + 2r) - 5m_Q - 2m_Q^{-1})\mathcal{W}_1(z)|$, is shown for $r = 1$ (blue) and $r = 0.5$ (orange). Its Green's function part, $|\text{Im}[W_{\beta,\alpha}^*(-2iy)W_{\beta,\alpha}(-2iz)]|$, for $y = 1$ is also plotted as the green line. In both panels we set $m_Q = 3.15$.

the non-linear source term from the first order tensor perturbations, $t_1^R \times t_1^R$. They are plotted in figure 10 for $r = 1$ and $r = 0.5$. Basically the second part is shifted by a factor of ≈ 2 along the z -axis, as r is reduced to the half. However, Green's function has a bigger amplitude at larger z without oscillations up to $z \simeq 10$. Note that the non-linear source term contains $\mathcal{W}_1(z) \equiv W_{\beta,\alpha}(-2ir_2z)W_{\beta,\alpha}(-2ir_3z)$, indicating that the two sourcing modes t_1^R have momenta $k_2 = k_3 = rk_1$ in the case of $r \equiv r_2 = r_3$, while the momentum of the sourced mode t_2^R is k_1 in the process of \mathcal{N}_1 . The fact that Green's function for t_2^R is larger on sub-horizon scales implies that the source effect from $t_1^R \times t_1^R$ to t_2^R is more efficient when the sourcing modes $t_1^R(rk_1)$ have lower momenta (i.e. a smaller r) and get amplified before $t_2^R(k_1)$ crosses the horizon. In other words, \mathcal{N}_1 becomes larger for a smaller r , because atypical Green's function G_t allows the sourcing effect to be active deep inside the horizon.

This non-linear sourcing process of t_2 through the diagram (i) shows clear contrast from the linear sourcing process from t_1 to ψ_1 discussed in section 3. There, Green's function for ψ , G_ψ , rapidly oscillates inside the horizon and does not allow t_1 to induce ψ_1 on sub-horizon scales, as shown in figure 1. In cases where only such normal Green's functions are involved, the shape of the bispectrum is typically equilateral, since all the modes are mainly produced around the horizon crossing. Nonetheless, in our case, Green's function for t_R is peculiar due to tachyonic instability, and the peak of the bispectrum deviates from the equilateral limit.

The total contribution to the bispectrum from \mathcal{N}_i and $\tilde{\mathcal{N}}_i$ is maximal in the folded limit $r = 0.5$. However, $\Xi(r_2, r_3)$ arising from the tensor polarisations is also an important factor determining the shape of the tensor bispectrum. Ξ is multiplied to the total bispectrum eq. (4.49) as an overall factor and it vanishes at $r_2 = r_3 = 0.5$. In figure 11, we illustrate how Ξ changes the shape of the bispectrum on the $r_2 = r_3$ plane. Ξ suppresses the bispectrum at lower r and vanishes at $r = 0.5$. In fact, Ξ vanishes not only at $r_2 = r_3 = 0.5$, but at all points on the line $r_2 + r_3 = 1$ (i.e. the folded limit), because of conservation of angular momentum. The Feynman diagrams in figure 2 can be seen as processes in which two spin-2 particles collide and one spin-2 particle comes out. In particular, in the case of a head-on collision, which corresponds to the folded limit, $k_2 + k_3 = k_1$, the cross-section vanishes, because the angular momentum is contributed only by spins (i.e. no orbital angular momentum) and the

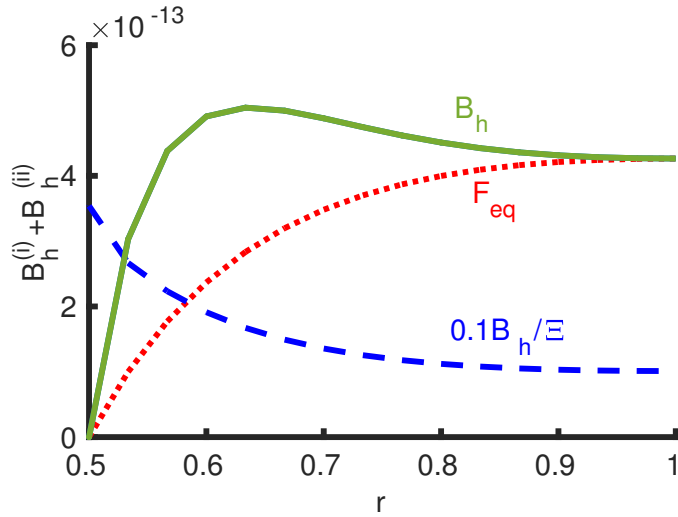


Figure 11: $(k_1 k_2 k_3)^2 (B_h^{(i)} + B_h^{(ii)})$ is plotted as solid green line as an function of $r \equiv r_2 = r_3$. The peak is located at $r \approx 0.6$ and the deviation from the equilateral shape (red dotted) is remarkable. The blue dashed line shows the case without Ξ , namely $10^{-1} (k_1 k_2 k_3)^2 (B_h^{(i)} + B_h^{(ii)}) / \Xi$ which is multiplied by 0.1 for illustrative purpose. The parameters are given in eq. (4.8).

spin of the system cannot be conserved as $2 \pm 2 \neq \pm 2$.

In summary, the peak of the tensor bispectrum B_h is located at $r \equiv r_2 = r_3 \approx 0.6$ for the following two reasons - (i) Among several contributions to the sourced tensor bispectrum B_h^{RRR} , the biggest one comes from $\langle \hat{\psi}_2^R(k_1) \hat{\psi}_1^R(k_2) \hat{\psi}_1^R(k_3) \rangle \propto \mathcal{N}_1$ in which the two linear perturbations of $SU(2)$ gauge field $\hat{t}_1^R(k = rk_1)$ non-linearly induce the second order one $\hat{t}_2^R(k_1)$ and subsequently $\hat{t}_2^R(k_1)$ sources the second order GW $\hat{\psi}_2^R(k_1)$. In this process, the amplitude of the second order fluctuations is larger when the momentum of the first order perturbations, rk_1 , is smaller, because in this case t_1^R gets amplified when the second order t_2^R is still deep inside the horizon where the source effect is more efficient (i.e. Green's function G_t has a bigger amplitude). Hence, \mathcal{N}_1 , which dominates the tensor bispectrum, is a decreasing function of r (see figure 10). (ii) The polarisation tensors also yield a r dependence as an overall factor $\Xi(r)$ to the total bispectrum. $\Xi(r)$ is a growing function of r and vanishes at $r = 0.5$. Multiplying $\Xi(r)$ changes the blue dashed line into the green line in figure 11. As the result of (i) and (ii), we obtain the bispectrum with a peak at $r \simeq 0.6$.

6 Parameter Search

In this section, we constrain the parameter regions from present observations and self-consistency of the model. We also clarify the parameter regions where the power spectrum or bispectrum of the sourced GWs will be detectable by upcoming CMB observations. Note that there remain four parameters, H, m_Q, ϵ_B and g , and one relationship $g^2 \epsilon_B M_{\text{P}}^2 = m_Q^4 H^2$. Eliminating g , we are left with three free parameters, H, m_Q and ϵ_B , in our model.

6.1 Tensor-to-scalar ratio

Currently the CMB observations put an upper bound on the tensor-to-scalar ratio r as

$$r \equiv \frac{P_h(k_{\text{CMB}})}{P_\zeta(k_{\text{CMB}})} < 0.07, \quad (95\% \text{ C.L.}), \quad (6.1)$$

where P_ζ is the power spectrum of the curvature perturbation and $k_{\text{CMB}} = 0.05 \text{ Mpc}^{-1}$. In our model, not only the vacuum fluctuation of the metric but also the sourced GWs contribute to P_h . Substituting eq. (3.18), the total tensor-to-scalar ratio is given as

$$r = \frac{\Delta_{\text{vac}}^h}{\Delta_\zeta} \left(1 + \frac{\epsilon_B}{2} |\mathcal{F}(m_Q)|^2 \right), \quad (6.2)$$

where the dimensionless scalar power spectrum, $\Delta_\zeta \equiv k^3 P_\zeta / 2\pi^2 \approx 2.2 \times 10^{-9}$ [42], and that of the tensor metric vacuum fluctuation, $\Delta_{\text{vac}}^h \equiv k^3 P_h^{\text{vac}} / 2\pi^2 = 2H^2 / \pi^2 M_{\text{P}}^2$, are introduced. Translating the upper bound on r into the constraint on our model parameters, we obtain

$$\epsilon_B < \left(\frac{0.07}{r_{\text{vac}}} - 1 \right) \frac{2}{|\mathcal{F}(m_Q)|^2}, \quad (6.3)$$

where the conventional tensor-to-scalar ratio contributed only from the tensor metric vacuum fluctuation is defined by

$$r_{\text{vac}} \equiv \frac{\Delta_{\text{vac}}^h}{\Delta_\zeta} \approx \frac{1}{2.2 \times 10^{-9}} \frac{2H^2}{\pi^2 M_{\text{P}}^2}. \quad (6.4)$$

Since the upcoming CMB B-mode polarisation observation missions aim to achieve a sensitivity $r \approx 10^3$, the parameter region predicting $r \geq 10^{-3}$ is particularly interesting. In our model, we find

$$r \geq 10^{-3} \iff \epsilon_B \geq \left(\frac{10^{-3}}{r_{\text{vac}}} - 1 \right) \frac{2}{|\mathcal{F}(m_Q)|^2}. \quad (6.5)$$

6.2 Tensor bispectrum

The constraint on the tensor bispectrum in the equilateral limit is also reported as a bound on $f_{\text{NL}}^{\text{tens}}$ [42],⁴

$$-1100 < f_{\text{NL}}^{\text{tens}} \equiv \frac{B_h^{\text{RRR}}(k, k, k)}{2\sqrt{2}F_\zeta^{\text{eq}}(k)} < 1900, \quad (68\% \text{ C.L.}), \quad (6.6)$$

where $B_h^{\text{RRR}}(k_1, k_2, k_3)$ is defined in eq. (4.1) and $F_\zeta^{\text{eq}}(k) \equiv (18/5)P_\zeta^2(k)$, evaluated at the pivot scale, $k_{\text{CMB}} = 0.05 \text{ Mpc}^{-1}$ [42]. Our model should satisfy these two observational constraints.

From the constraint on $f_{\text{NL}}^{\text{tens}}$ we find,

$$\epsilon_B \geq \frac{64 M_{\text{Pl}}^4}{27 H^4} \frac{1100 \cdot 18 \cdot \Delta_\zeta^2 \cdot 4\pi^4 \cdot 2\sqrt{2}}{-5 \cdot \Upsilon_{\text{eq}}(m_Q)}, \quad (6.7)$$

$$\epsilon_B \leq \frac{64 M_{\text{Pl}}^4}{27 H^4} \frac{1900 \cdot 18 \cdot \Delta_\zeta^2 \cdot 4\pi^4 \cdot 2\sqrt{2}}{5 \cdot \Upsilon_{\text{eq}}(m_Q)}, \quad (6.8)$$

where the first constraint applies when $\Upsilon_{\text{eq}} < 0$ and the second when $\Upsilon_{\text{eq}} > 0$.

⁴The factor of $2\sqrt{2}$ in the denominator comes from the difference of the normalisation of the polarisation tensors. In [42], $e_{ij}^R(\mathbf{k})e_{ij}^R(-\mathbf{k}) = 2$ is adopted.

6.3 Consistency of the model

In addition to these observational constraints, we discuss the restriction imposed by self-consistency of the model. Scalar perturbations of the spectator sector have a fatal instability on sub-horizon scale if $m_Q < \sqrt{2}$ [35]. Hence we demand $m_Q > \sqrt{2}$ in our model. Since ϵ_B approximately indicates the energy density fraction of the background SU(2) gauge field,

$$\Omega_A \equiv \frac{\rho_Q}{3M_{\text{P}}^2 H^2} = \frac{(\dot{Q} + HQ)^2 + g^2 Q^4}{2M_{\text{P}}^2 H^2} \simeq \frac{1 + m_Q^2}{2m_Q^2} \epsilon_B, \quad (6.9)$$

ϵ_B is positive and small. As found in [43], if ϵ_B is too large, its effect on the evolution of the inflaton perturbation significantly alters the spectral index n_s , because ϵ_B contributes to \dot{H} through eq. (2.11). To keep this effect negligible, it is required

$$\epsilon_B(t_*) < 2 \times 10^{-2}, \quad (6.10)$$

where t_* is the time at which CMB modes leave the horizon. On the other hand, since ϵ_B can be rewritten as $\epsilon_B = m_Q^4 H^2 / (g^2 M_{\text{P}}^2)$, if one lowers ϵ_B by fixing m_Q and H , one would confront a large self-coupling constant g of the SU(2) gauge fields which leads to a non-negligible backreaction from $SU(2)$ tensor perturbations to the background dynamics. In order to avoid large backreaction, we need to have [20]

$$\epsilon_B > \frac{m_Q^2 [\mathcal{B} + \tilde{\mathcal{B}} / (m_Q + m_Q^{-1})]}{24\pi^2} \left(\frac{H}{M_{\text{P}}} \right)^2, \quad (6.11)$$

where \mathcal{B} and $\tilde{\mathcal{B}}$ are functions of m_Q given by

$$\mathcal{B}(m_Q) = \int_0^{x_{\text{max}}} dx x \left| i^\beta W_{\beta,\alpha}(-2ix) \right|^2, \quad \tilde{\mathcal{B}}(m_Q) = \int_0^{x_{\text{max}}} dx x^2 \left| i^\beta W_{\beta,\alpha}(-2ix) \right|^2. \quad (6.12)$$

We also find that equation (6.11) ensures $g \ll 1$ as well, which is preferred for validity of the perturbation series.⁵

6.4 Allowed parameter regions

Equations (6.1)–(6.11), together with $m_Q > \sqrt{2}$, give the set of constraints we employ to define the regions in ϵ_B – m_Q plane that are interesting for future CMB experiments. Figures (12)–(14) show the allowed regions for 3 different choices of H or equivalently $r_{\text{vac}} = 10^{-4}$, 10^{-3} and 10^{-2} . As r_{vac} increases, the allowed parameter space shrinks. This is because the upper bound on r implies that the power in the sourced tensor modes cannot be very large if r_{vac} is large.

The bottom right corners in these figures (i.e. regions with a large m_Q and small ϵ_B) are shaded as the parameter spaces with non-negligible backreaction, although this does not mean that these regions are excluded. Rather, it indicates that one needs to perform numerical calculations to take into account backreaction, to study this parameter space [20] (see ref. [43] where the backreaction is numerically incorporated).

We find that there's a general trend in the constraining power of tensor power spectrum and bispectrum. While the power spectrum is better at constraining small m_Q regions,

⁵Strictly speaking, since our setup does not include any $SU(2)$ charged particle, a large g itself is not necessarily problematic. However, if one considers a charged particle, $g \gtrsim 1$ causes a strong coupling problem in that loop effects would alter dynamics of the SU(2) gauge fields.

the bispectrum is better at constraining large m_Q regions. This happens because B_h is exponentially more sensitive to m_Q (it has an extra factor of $e^{2\pi(2m_Q+m_Q^{-1})}$ compared to r), and so, a small change in m_Q can easily change B_h by a large factor ($\sim e^{4\pi\Delta m_Q}$). This also has interesting consequences for detectability of the tensor bispectrum, as a large range of bispectra can be generated even for the small range of values of interest, $\sqrt{2} < m_Q \lesssim 4$, making a detection of the tensor bispectrum (in this model) possible in the near future, even if r is small (see figures (12)–(14)). While even the current constraints on $f_{\text{NL}}^{\text{tens}}$ are useful for ruling out the top right corners in the figures (i.e. regions with a large m_Q and large ϵ_B), there remains parameter space in which the tensor bispectrum can be observed in the future. It is then natural to ask what range of parameters can be probed in upcoming CMB missions.

To that end we also plot the line for $\sigma(f_{\text{NL}}^{\text{tens}}) = 1$ in figures (12)–(14), which is expected to be the target sensitivity of LiteBIRD (M. Shiraishi, private communication). We see that this improved sensitivity will allow us to probe a significant portion of the parameter space with large m_Q and small ϵ_B , which is inaccessible to measurements of r , even if we can measure $r = 10^{-4}$ (figure 12, bottom right). Although our present calculation does not ensure that this conclusion stays unchanged when we account for the backreaction, it might still be true when backreaction is included. We also show the line corresponding to $r_{\text{source}} = r_{\text{vac}}$. Regions to the left of this line denote regions where the amplitude of the sourced tensor modes is smaller than the amplitude of vacuum tensor of the metric. From figure 14 we see that if $r_{\text{vac}} = 10^{-2}$, there is a region of intermediate ϵ_B and m_Q values for which $f_{\text{NL}}^{\text{tens}} > 1$, also if $r_{\text{source}} < r_{\text{vac}}$. This regime is particularly interesting because one can learn about both vacuum fluctuations of the metric and spectator fields during inflation, by combining the power spectrum and bispectrum. On the other hand, if r_{vac} is smaller, a small r_{source} is accompanied by a small tensor bispectrum as well.

7 Conclusion

In this paper we have calculated the bispectrum of tensor perturbations sourced by spectator SU(2) gauge fields during inflation [20]. The primary contribution to the bispectrum comes from the self-interaction of the SU(2) gauge fields; thus, it is unique to non-Abelian gauge theory. We find that the amplitude of the bispectrum parametrised by its ratio to the (squared) power spectrum, B_h/P_h^2 , is very large, $\sim 1/\epsilon_B$ [30]. Since $\epsilon_B \ll 1$, this is much larger than ~ 1 which is predicted for quantum fluctuations of the metric [31, 32].

We also explored parameter space of the model relevant to future CMB missions. Even with an r_{vac} as low as 10^{-4} , large parameter space remains consistent theoretically as well as with the current CMB observations. However, the exponential sensitivity of the power spectrum and bispectrum on model parameters makes it difficult to completely eliminate all the parameter space of the model on the basis of just these observations.

Upcoming CMB missions such as LiteBIRD [44] will measure the CMB polarisation to unprecedented accuracy. This will allow us to not only detect B-modes but also to characterise them, hence testing one of our most ambitious claims about our origins. If the primordial B-modes arise from quantum fluctuations of the metric, we will find them to be parity invariant, near scale-invariant, and weakly non-Gaussian. If not, we will use the deviations to constrain the fraction of energy density in spectator gauge fields in the inflationary Universe [25, 30, 45, 46].

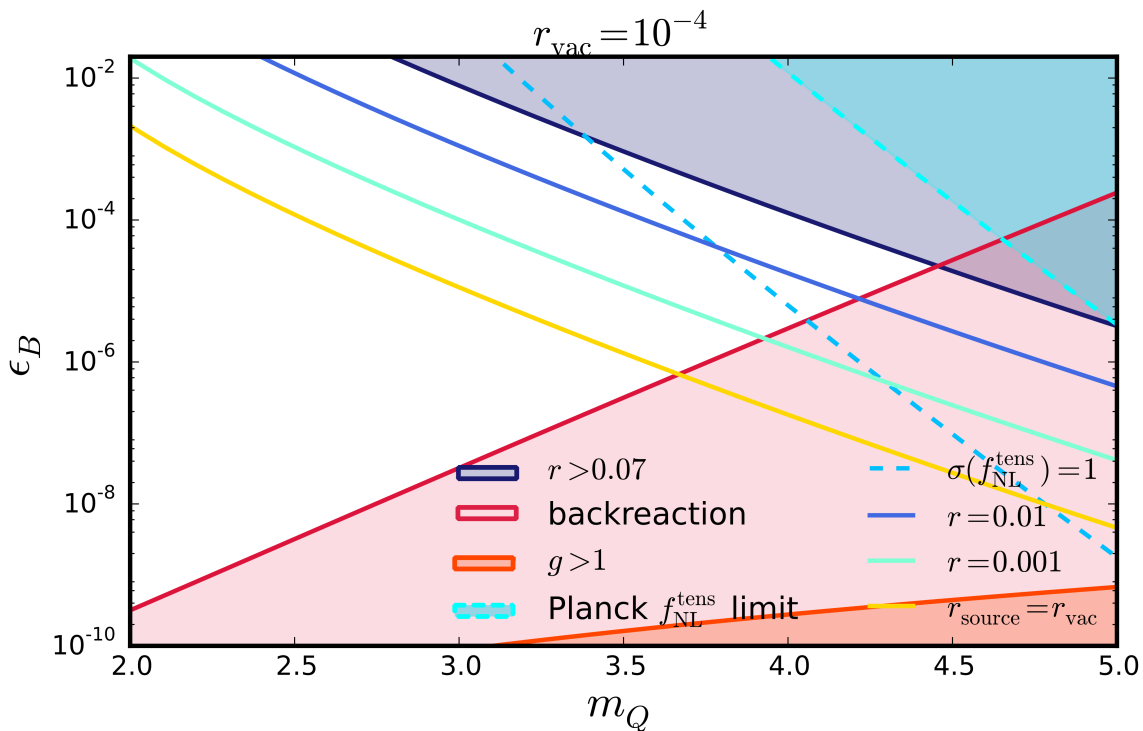


Figure 12: Parameter space for gravitational wave production in our model, for $r_{\text{vac}} = 10^{-4}$, and for scale-invariant GWs. The blue and magenta shaded regions are excluded by the current upper bound on $f_{\text{NL}}^{\text{tens}}$ and r [42], respectively. The light red shaded region is not necessarily ruled out but a significant backreaction requires a dedicated numerical treatment to obtain the predictions. In the orange shaded region, the system confronts a strong coupling problem, if one considers $SU(2)$ charged particle. We also show $f_{\text{NL}}^{\text{tens}} = 1$ as the dashed blue line, because an error of order unity $\sigma(f_{\text{NL}}^{\text{tens}}) \sim 1$ would be achieved by upcoming CMB B-mode missions. The solid lines denote $r = 10^{-2}$ (blue), 10^{-3} (green) and 10^{-4} (yellow).

Acknowledgments

We would like to thank M. Shiraishi and R. Namba for useful discussions.

A Polarisation Tensor

In this appendix, we construct the left and right-handed transverse and traceless polarisation tensors. We start with the left and right-handed polarisation vector whose wave number is parallel to the z-axis,

$$\epsilon^{L/R}(\hat{z}) = \frac{1}{\sqrt{2}} \begin{pmatrix} 1 \\ \pm i \\ 0 \end{pmatrix}. \quad (\text{A.1})$$

The plus and minus signs are for left- (L) and right-handed (R) polarisation vectors, respectively. From now on, \pm means $+$ for L and $-$ for R , whereas \mp means $-$ for L and $+$ for R . To obtain the polarisation vector with a general wave number $\hat{\mathbf{k}}$ which points in the direction

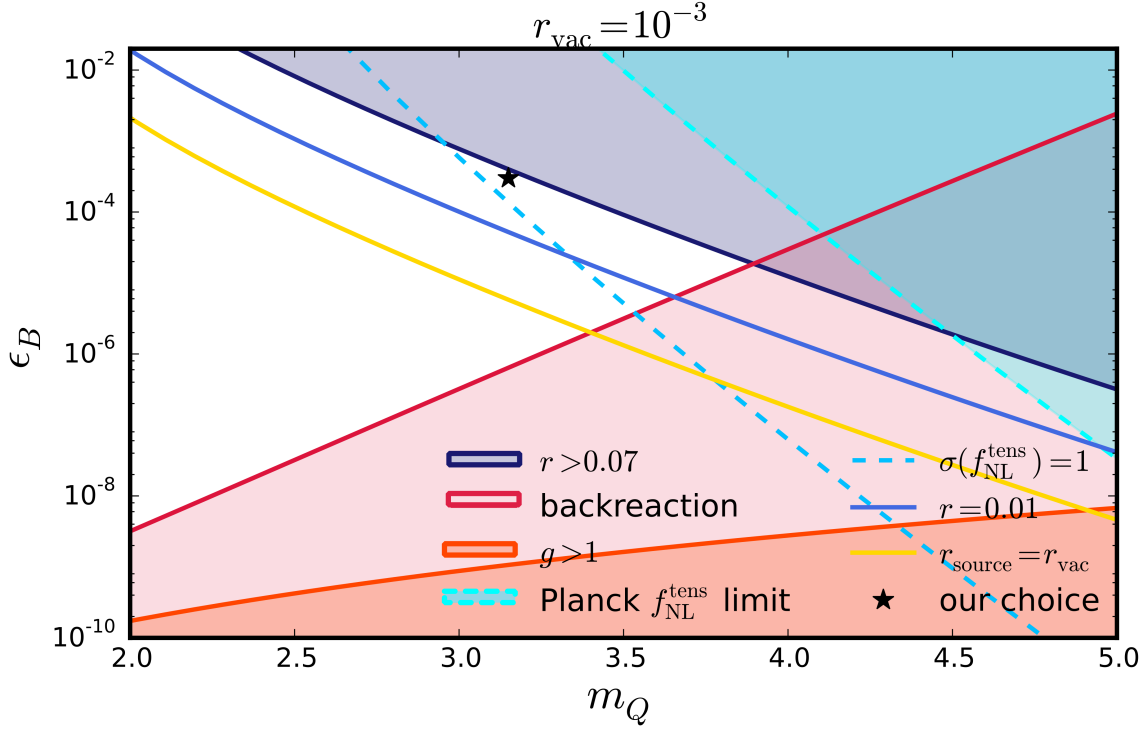


Figure 13: Same as figure 12 but for $r_{\text{vac}} = 10^{-3}$. The black star denotes the parameter choice given in eq. (4.8).

of (θ, φ) in polar coordinate, we use the following rotation matrix which transforms \hat{z} into \hat{k} :

$$S(\hat{\mathbf{k}}) = \begin{pmatrix} \cos \theta \cos \varphi & -\sin \varphi & \sin \theta \cos \varphi \\ \cos \theta \sin \varphi & \cos \varphi & \sin \theta \sin \varphi \\ -\sin \theta & 0 & \cos \theta \end{pmatrix}. \quad (\text{A.2})$$

Then we find

$$\epsilon^{L/R}(\hat{\mathbf{k}}) = S(\hat{\mathbf{k}})\epsilon^{L/R}(\hat{z}) = \frac{1}{\sqrt{2}} \begin{pmatrix} \cos \theta \cos \varphi \mp i \sin \varphi \\ \cos \theta \sin \varphi \pm i \cos \varphi \\ -\sin \theta \end{pmatrix}. \quad (\text{A.3})$$

These polarisation vectors satisfy

$$\begin{aligned} \mathbf{k} \cdot \epsilon^{L/R}(\hat{\mathbf{k}}) &= 0, & \epsilon^{L/R*}(\hat{\mathbf{k}}) &= \epsilon^{R/L}(\hat{\mathbf{k}}) = \epsilon^{L/R}(-\hat{\mathbf{k}}), \\ \epsilon^{L/R}(\hat{\mathbf{k}}) \cdot \epsilon^{R/L}(\hat{\mathbf{k}}) &= 1, & \epsilon^{L/R}(\hat{\mathbf{k}}) \cdot \epsilon^{L/R}(\hat{\mathbf{k}}) &= 0. \end{aligned} \quad (\text{A.4})$$

The polarisation tensor $e_{ij}^{L/R}(\hat{\mathbf{k}})$ can be constructed from the polarisation vectors,

$$e_{ij}^{L/R}(\hat{\mathbf{k}}) = \epsilon_i^{L/R}(\hat{\mathbf{k}}) \epsilon_j^{L/R}(\hat{\mathbf{k}}). \quad (\text{A.5})$$

These polarisation tensors are transverse and traceless and satisfy

$$e_{ij}^L(-\hat{\mathbf{k}}) = e_{ij}^{L*}(\hat{\mathbf{k}}) = e_{ij}^R(\hat{\mathbf{k}}), \quad i\epsilon_{ijk}k_i e_{jl}^{L/R}(\hat{\mathbf{k}}) = \pm k e_{kl}^{L/R}(\hat{\mathbf{k}}), \quad e_{ij}^L(\hat{z}) = \frac{1}{2} \begin{pmatrix} 1 & i & 0 \\ i & -1 & 0 \\ 0 & 0 & 0 \end{pmatrix}. \quad (\text{A.6})$$

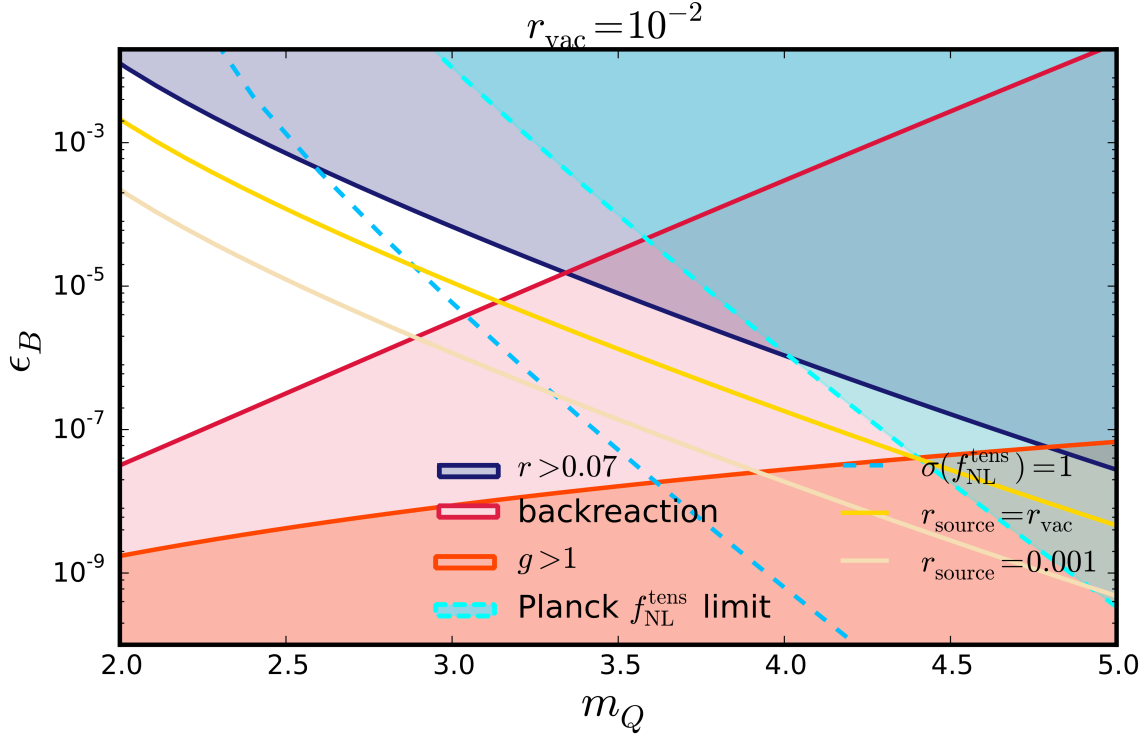


Figure 14: Same as figure 12 but for $r_{\text{vac}} = 10^{-2}$.

Although the general expression for $e_{ij}^{L/R}(\hat{\mathbf{k}})$ is rather complicated, we can fix θ in the current case. This is because we calculate three polarisation tensors with three different wavenumbers, $e_{ij}^R(\hat{\mathbf{k}}_1)e_{kl}^R(\hat{\mathbf{k}}_2)e_{nm}^R(\hat{\mathbf{k}}_3)$ whose indices are somehow contracted, and these wave vectors are on the same plane due to momentum conservation, $\delta(\mathbf{k}_1 + \mathbf{k}_2 + \mathbf{k}_3)$. In that case, we can set $\theta = \pi/2$ and let these vectors, $\mathbf{k}_1, \mathbf{k}_2, \mathbf{k}_3$, move only on the x-y plane. For $\theta = \pi/2$, the polarisation tensors become

$$e_{ij}^{L/R}\left(\theta = \frac{\pi}{2}, \varphi\right) = \frac{1}{2} \begin{pmatrix} -\sin^2 \varphi & \cos \varphi \sin \varphi & \pm i \sin \varphi \\ \cos \varphi \sin \varphi & -\cos^2 \varphi & \mp i \cos \varphi \\ \pm i \sin \varphi & \mp i \cos \varphi & 1 \end{pmatrix}. \quad (\text{A.7})$$

Now we have three angles, $\varphi_1, \varphi_2, \varphi_3$, associated with wavenumbers, $\mathbf{k}_1, \mathbf{k}_2, \mathbf{k}_3$, respectively. Without loss of generality, we can set $\varphi_1 = 0$. Furthermore, these trigonometric functions of φ_2 and φ_3 can be rewritten as functions of $r_2 \equiv k_2/k_1$ and $r_3 \equiv k_3/k_1$. Using $\mathbf{k}_1 + \mathbf{k}_2 + \mathbf{k}_3 = 0$, we find

$$k_3^2 = |\mathbf{k}_1 + \mathbf{k}_2|^2 = k_1^2 + k_2^2 + 2k_1k_2 \cos \varphi_2 \implies \cos \varphi_2 = \frac{r_3^2 - r_2^2 - 1}{2r_2}. \quad (\text{A.8})$$

In the same way, we also find $\cos \varphi_3 = (r_2^2 - r_3^2 - 1)/(2r_3)$. With this notation, we find

$$\sum_{\{I,J,K\}}^{\{1,2,3\}} i \epsilon^{abc} k_K^i e_{ai}^R(\hat{\mathbf{k}}_I) e_{bj}^R(\hat{\mathbf{k}}_J) e_{cj}^R(\hat{\mathbf{k}}_K) = -2k_1 \Xi \tilde{\Xi}, \quad (\text{A.9})$$

$$e_{ij}^R(\hat{\mathbf{k}}_1) e_{jl}^R(\hat{\mathbf{k}}_2) e_{li}^R(\hat{\mathbf{k}}_3) = \Xi, \quad \epsilon^{abc} \epsilon^{ijk} e_{ai}^R(\hat{\mathbf{k}}_1) e_{bj}^R(\hat{\mathbf{k}}_2) e_{ck}^R(\hat{\mathbf{k}}_3) = 2\Xi, \quad (\text{A.10})$$

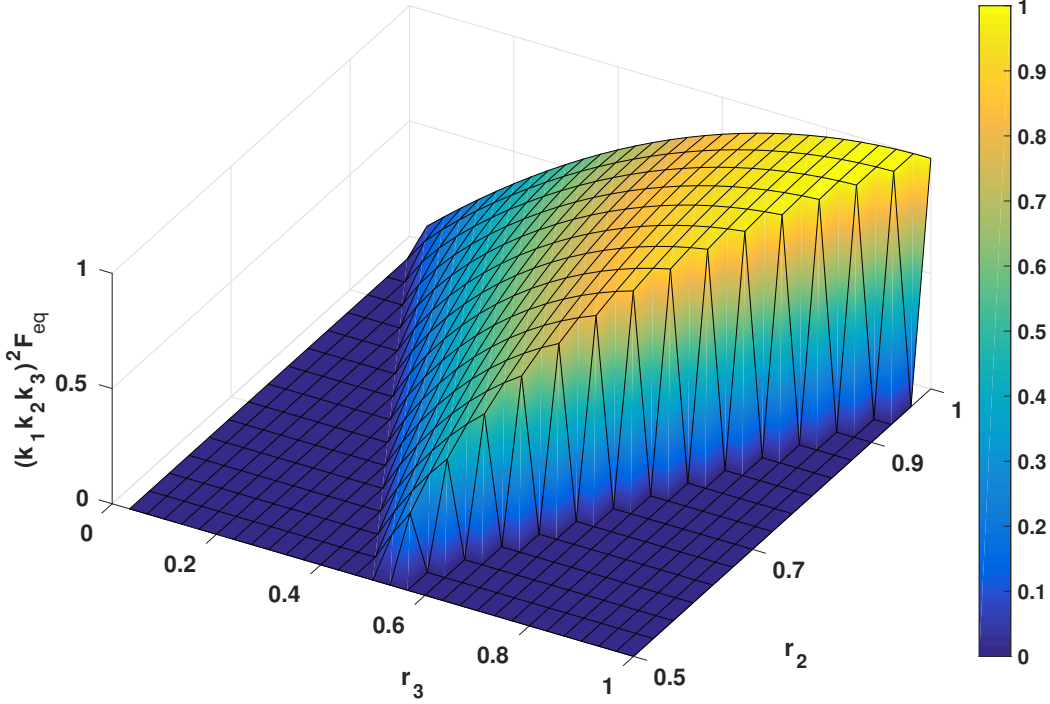


Figure 15: 3D plot of $(k_1 k_2 k_3)^2 F_{\text{eq}}$, equation (B.3).

where

$$\Xi \equiv \frac{(1 + r_2 + r_3)^3}{64 r_2^2 r_3^2} (r_2 + r_3 - 1)(1 + r_2 - r_3)(1 + r_3 - r_2), \quad (\text{A.11})$$

$$\tilde{\Xi} \equiv 1 + r_2 + r_3. \quad (\text{A.12})$$

$\sum_{\{I,J,K\}}^{\{1,2,3\}}$ denotes summation of all the permutation, $\{I, J, K\} = \{\text{Perm}(1, 2, 3)\}$.

B Equilateral Shape

To measure similarity of the shapes of bispectra, the cosine between two shapes is introduced as [40],

$$\cos(B_h, F_{\text{ref}}) \equiv \frac{B_h \cdot F_{\text{ref}}}{\sqrt{(B_h \cdot B_h)(F_{\text{ref}} \cdot F_{\text{ref}})}}, \quad (\text{B.1})$$

where the dot product is defined as

$$X \cdot Y \equiv \int_0^1 dr_2 \int_0^1 dr_3 (r_2 r_3)^4 X(1, r_2, r_3) Y(1, r_2, r_3). \quad (\text{B.2})$$

Here F_{ref} is the reference template to which the similarity is measured. In this paper we use the equilateral template [47]

$$F_{\text{eq}}(k_1, k_2, k_3) = \left[-\frac{1}{k_1^3 k_2^3} - \frac{1}{k_1^3 k_3^3} - \frac{1}{k_2^3 k_3^3} - \frac{2}{k_1^2 k_2^2 k_3^2} + \frac{1}{k_1 k_2^2 k_3^2} + (5 \text{ perm}) \right]. \quad (\text{B.3})$$

Figure 15 shows the shape of this template as a function of r_2 and r_3 .

References

- [1] L. P. Grishchuk, Amplification of gravitational waves in an isotropic universe, *Sov. Phys. JETP* **40** (1975) 409–415.
- [2] A. A. Starobinsky, Spectrum of relict gravitational radiation and the early state of the universe, *JETP Lett.* **30** (1979) 682–685.
- [3] U. Seljak and M. Zaldarriaga, Signature of gravity waves in polarization of the microwave background, *Phys. Rev. Lett.* **78** (1997) 2054–2057, [[astro-ph/9609169](#)].
- [4] M. Kamionkowski, A. Kosowsky and A. Stebbins, A Probe of primordial gravity waves and vorticity, *Phys. Rev. Lett.* **78** (1997) 2058–2061, [[astro-ph/9609132](#)].
- [5] BICEP2, KECK ARRAY collaboration, P. A. R. Ade et al., Improved Constraints on Cosmology and Foregrounds from BICEP2 and Keck Array Cosmic Microwave Background *Phys. Rev. Lett.* **116** (2016) 031302, [[1510.09217](#)].
- [6] J. L. Cook and L. Sorbo, Particle production during inflation and gravitational waves detectable by ground-based interferometers, *Phys. Rev.* **D85** (2012) 023534, [[1109.0022](#)].
- [7] D. Carney, W. Fischler, E. D. Kovetz, D. Lorshbough and S. Paban, Rapid field excursions and the inflationary tensor spectrum, *JHEP* **11** (2012) 042, [[1209.3848](#)].
- [8] M. Biagetti, M. Fasiello and A. Riotto, Enhancing Inflationary Tensor Modes through Spectator Fields, *Phys. Rev.* **D88** (2013) 103518, [[1305.7241](#)].
- [9] L. Senatore, E. Silverstein and M. Zaldarriaga, New Sources of Gravitational Waves during Inflation, *JCAP* **1408** (2014) 016, [[1109.0542](#)].
- [10] L. Sorbo, Parity violation in the Cosmic Microwave Background from a pseudoscalar inflaton, *JCAP* **1106** (2011) 003, [[1101.1525](#)].
- [11] M. M. Anber and L. Sorbo, Non-Gaussianities and chiral gravitational waves in natural steep inflation, *Phys. Rev.* **D85** (2012) 123537, [[1203.5849](#)].
- [12] N. Barnaby and M. Peloso, Large Nongaussianity in Axion Inflation, *Phys. Rev. Lett.* **106** (2011) 181301, [[1011.1500](#)].
- [13] N. Barnaby, J. Moxon, R. Namba, M. Peloso, G. Shiu and P. Zhou, Gravity waves and non-Gaussian features from particle production in a sector gravitationally coupled to the inflaton *Phys. Rev.* **D86** (2012) 103508, [[1206.6117](#)].
- [14] M. Peloso, L. Sorbo and C. Unal, Rolling axions during inflation: perturbativity and signatures, *JCAP* **1609** (2016) 001, [[1606.00459](#)].
- [15] A. Maleknejad and M. M. Sheikh-Jabbari, Gauge-flation: Inflation From Non-Abelian Gauge Fields, *Phys. Lett.* **B723** (2013) 224–228, [[1102.1513](#)].
- [16] E. Dimastrogiovanni and M. Peloso, Stability analysis of chromo-natural inflation and possible evasion of Lyths bound, *Phys. Rev.* **D87** (2013) 103501, [[1212.5184](#)].

- [17] P. Adshead, E. Martinec and M. Wyman, Perturbations in Chromo-Natural Inflation, [JHEP](#) **09** (2013) 087, [[1305.2930](#)].
- [18] P. Adshead, E. Martinec and M. Wyman, Gauge fields and inflation: Chiral gravitational waves, fluctuations, and the Lyth bound, [Phys. Rev. D](#) **88** (2013) 021302, [[1301.2598](#)].
- [19] A. Maleknejad, Axion Inflation with an SU(2) Gauge Field: Detectable Chiral Gravity Waves, [JHEP](#) **07** (2016) 104, [[1604.03327](#)].
- [20] E. Dimastrogiovanni, M. Fasiello and T. Fujita, Primordial Gravitational Waves from Axion-Gauge Fields Dynamics, [JCAP](#) **1701** (2017) 019, [[1608.04216](#)].
- [21] R. R. Caldwell and C. Devulder, Axion Gauge Field Inflation and Gravitational Leptogenesis: A Lower Bound on B Modes from the Matter-Antimatter Asymmetry, [Phys. Rev. D](#) **97** (2018) 023532, [[1706.03765](#)].
- [22] P. Adshead, E. Martinec, E. I. Sfakianakis and M. Wyman, Higgsed Chromo-Natural Inflation, [JHEP](#) **12** (2016) 137, [[1609.04025](#)].
- [23] M. Kamionkowski and E. D. Kovetz, The Quest for B Modes from Inflationary Gravitational Waves, [Ann. Rev. Astron. Astrophys.](#) **54** (2016) 227–269, [[1510.06042](#)].
- [24] S. Saito, K. Ichiki and A. Taruya, Probing polarization states of primordial gravitational waves with CMB anisotropies, [JCAP](#) **0709** (2007) 002, [[0705.3701](#)].
- [25] R. Namba, M. Peloso, M. Shiraishi, L. Sorbo and C. Unal, Scale-dependent gravitational waves from a rolling axion, [JCAP](#) **1601** (2016) 041, [[1509.07521](#)].
- [26] B. Thorne, T. Fujita, M. Hazumi, N. Katayama, E. Komatsu and M. Shiraishi, Finding the chiral gravitational wave background of an axion-SU(2) inflationary model using CMB observations and BICEP2, [JCAP](#) **1707** (2017) 03240.
- [27] A. Lue, L.-M. Wang and M. Kamionkowski, Cosmological signature of new parity violating interactions, [Phys. Rev. Lett.](#) **83** (1999) 1506–1509, [[astro-ph/9812088](#)].
- [28] V. Gluscevic and M. Kamionkowski, Testing Parity-Violating Mechanisms with Cosmic Microwave Background Experiments, [Phys. Rev. D](#) **81** (2010) 123529, [[1002.1308](#)].
- [29] M. Gerbino, A. Gruppuso, P. Natoli, M. Shiraishi and A. Melchiorri, Testing chirality of primordial gravitational waves with Planck and future CMB data: no hope from angular power spectrum, [JCAP](#) **1607** (2016) 044, [[1605.09357](#)].
- [30] A. Agrawal, T. Fujita and E. Komatsu, Large Tensor Non-Gaussianity from Axion-Gauge Fields Dynamics, [JCAP](#) **1707** (2017) 03023.
- [31] J. M. Maldacena, Non-Gaussian features of primordial fluctuations in single field inflationary models, [JHEP](#) **05** (2003) 013, [[astro-ph/0210603](#)].
- [32] J. M. Maldacena and G. L. Pimentel, On graviton non-Gaussianities during inflation, [JHEP](#) **09** (2011) 045, [[1104.2846](#)].
- [33] P. Adshead and M. Wyman, Chromo-Natural Inflation: Natural inflation on a steep potential with classical non-Abelian gauge fields, [Phys. Rev. Lett.](#) **108** (2012) 261302, [[1202.2366](#)].

- [34] A. Maleknejad and E. Erfani, Chromo-Natural Model in Anisotropic Background, [JCAP](#) **1403** (2014) 016, [[1311.3361](#)].
- [35] E. Dimastrogiovanni and M. Peloso, Stability analysis of chromo-natural inflation and possible evasion of Lyths bound, [Phys. Rev. D](#) **87** (2013) 103501, [[1212.5184](#)].
- [36] D. H. Lyth and D. Wands, Generating the curvature perturbation without an inflaton, [Phys. Lett. B](#) **524** (2002) 5–14, [[hep-ph/0110002](#)].
- [37] D. H. Lyth, C. Ungarelli and D. Wands, The Primordial density perturbation in the curvaton scenario, [Phys. Rev. D](#) **67** (2003) 023503, [[astro-ph/0208055](#)].
- [38] I. Obata and J. Soda, Chiral primordial gravitational waves from dilaton induced delayed chromonatural inflation, [Phys. Rev. D](#) **93** (2016) 123502, [[1602.06024](#)].
- [39] D. Seery, K. A. Malik and D. H. Lyth, Non-gaussianity of inflationary field perturbations from the field equation, [JCAP](#) **0803** (2008) 014, [[0802.0588](#)].
- [40] D. Babich, P. Creminelli and M. Zaldarriaga, The Shape of non-Gaussianities, [JCAP](#) **0408** (2004) 009, [[astro-ph/0405356](#)].
- [41] WMAP collaboration, E. Komatsu et al., First year Wilkinson Microwave Anisotropy Probe (WMAP) observations: tests of gaussianity, [Astrophys. J. Suppl.](#) **148** (2003) 119–134, [[astro-ph/0302223](#)].
- [42] PLANCK collaboration, P. A. R. Ade et al., Planck 2015 results. XIII. Cosmological parameters, [Astron. Astrophys.](#) **594** (2016) A13, [[1502.01589](#)].
- [43] T. Fujita, R. Namba and Y. Tada, Does the detection of primordial gravitational waves exclude low energy inflation?, [Phys. Lett. B](#) **778** (2018) 17–21, [[1705.01533](#)].
- [44] T. Matsumura et al., Mission design of LiteBIRD, [J. Low. Temp. Phys.](#) **176** (2014) 733, [[1311.2847](#)].
- [45] J. L. Cook and L. Sorbo, An inflationary model with small scalar and large tensor nongaussianities, [JCAP](#) **1311** (2013) 047, [[1307.7077](#)].
- [46] M. Shiraishi, C. Hikage, R. Namba, T. Namikawa and M. Hazumi, Testing statistics of the CMB B -mode polarization toward unambiguously establishing quantum fluctuation of the [Phys. Rev. D](#) **94** (2016) 043506, [[1606.06082](#)].
- [47] P. Creminelli, A. Nicolis, L. Senatore, M. Tegmark and M. Zaldarriaga, Limits on non-gaussianities from wmap data, [JCAP](#) **0605** (2006) 004, [[astro-ph/0509029](#)].